Review Article Vol. 5, No. 12 / December 2018 / Optica 1564

Ultra-precise timing and synchronization for large-scale scientific instruments

Ming Xin,[1,*] Kemal Şafak,[1,2] and Franz X. Kärtner[1,3]

[1]Center for Free-Electron Laser Science, Deutsches Elektronen-Synchrotron, Hamburg 22607, Germany
[2]Cycle GmbH, Hamburg 22607, Germany
[3]Department of Physics and the Hamburg Center for Ultrafast Imaging, University of Hamburg, Hamburg 22761, Germany
*Corresponding author: ming.xin@desy.de

Received 11 September 2018; revised 3 November 2018; accepted 13 November 2018 (Doc. ID 345607); published 5 December 2018

Ultra-precise timing has become a prerequisite for many modern large-scale scientific instruments, and timing precision is a crucial enabling factor to achieve the ultimate goals of those instruments. Here, we review the recent progress in timing technologies, including timing characterization methods among different kinds of sources (optical lasers, microwaves and x-ray pulses), large-scale free-space timing synchronization, and fiber-based timing synchronization. Technical and fundamental limitations of fiber-based timing systems are also discussed to provide future directions.

https://doi.org/10.1364/OPTICA.5.001564

1. INTRODUCTION

With the advent of mode-locked lasers [1] and optical frequency combs [2,3], the precision of timing metrology has dramatically increased. Ultra-precise timing technologies are playing an increasingly important role in modern large-scale scientific facilities. For example, attosecond precision timing distribution systems are required urgently in X-ray free-electron lasers (XFELs). Several XFELs, including the European XFEL [4] in Hamburg, FERMI [5] in Italy, SwissFEL in Switzerland, Linac Coherent Light Source (LCLS) [6] and LCLS II [7] at Stanford are built or being built to ultimately generate attosecond (as) x-ray pulses [8] with unprecedented brightness to film chemical and physical reactions with subatomic-level spatiotemporal resolution [9,10]. In the past few years, significant progress has been made in the field of ultrafast molecular imaging, such as the time-domain observation of intramolecular charge transfer [11] and the discovery of ultrafast Auger processes altering the chemistry of matter on an attosecond time scale [12,13]. However, the current XFELs are still not using their full potential for subatomic-level movie applications due to the lack of an attosecond-precision timing control to avoid blurring of the individual images in time. In order to generate attosecond x-ray pulses, all the optical and microwave subsources inside an XFEL, including the electron gun, injector laser, microwave references of the linear accelerators, bunch compressor, and the seed laser need to be synchronized simultaneously with attosecond relative timing jitter. Furthermore, accurate measurements of the relative timing between the x-ray pump and the optical probe pulses at the end station are also required to perform attosecond-precision pump-probe experiments. Therefore, a multikilometer timing distribution system synchronizing microwave, optical, and x-ray sources with attosecond precision is imperative to unleash the full potential of these billion-dollar photon science facilities.

In addition to XFELs, ultrahigh peak-power laser facilities also attract worldwide interest. For example, extreme light infrastructure (ELI) [14] is designed to be the first exawatt-class (10^{18} W) laser with 10-fs pulse duration. Such a source of highly intense and short pulses can be used in laser-based nuclear physics [15], hadron therapy, attoscience, strong-field laser physics, and many other interdisciplinary studies. Within these sources, optical parametric chirped-pulse amplification (OPCPA)-based pump lasers also need to be synchronized with a precision of ~10 fs. There are also new and promising laser concepts emerging to generate both high average and peak powers. For instance, researchers aim to combine thousands of pulsed fiber lasers coherently, which could be the driving force behind next-generation particle accelerators [16]. To make this happen, the relative phase differences between adjacent fibers must be within $\lambda/100$ (where λ is the wavelength), which corresponds to a timing control with 10-as level precision.

Furthermore, ambitious multitelescope array projects [17–20] require 10^{-6} arcsec angular resolution (corresponding to 50-km spatial resolution at 1-light-year distance) for cosmic imaging in order to obtain the surface details of distant astronomical objects, especially to explore exoplanets in the habitable zone. To achieve this goal, the telescope array has to work at terahertz or optical wavelengths [19] spanning over hundreds-of-kilometers distance, and femtosecon/attosecond/-precision synchronization must be ensured among the individual telescopes to perform an accurate phase correlation of the ultrafast detected signals.

In brief, femtosecond or higher timing precision is desirable for these scientific instruments to attain their ultimate scientific purposes. In this paper, we will review different cutting-edge timing technologies used in large-scale scientific instruments. In

Section 2, we first present timing characterization methods for different sources, including optical lasers, microwaves, and x-rays. Sections 3 and 4 focus on the free-space-based and fiber-based timing systems, respectively. Finally, we discuss plausible future directions of timing in Section 5.

2. TIMING CHARACTERIZATION

Timing is a particular point or period in time when something happens. Timing characterization comprises two fundamental tasks: how to define the timing and how to measure the timing. Generally, the timing information of an electromagnetic pulse can be defined by its temporal center of gravity (COG):

$$T_{\mathrm{COG}} = \int_{-\infty}^{+\infty} t|E(t)|^2 \mathrm{d}t \Big/ \int_{-\infty}^{+\infty} |E(t)|^2 \mathrm{d}t, \tag{1}$$

where $E(t)$ is the electric field of the pulse. The merit of this definition is that the timing can be extracted from power measurement. In contrast, if the timing is defined as the time of pulse peak position, it would be extremely difficult to measure it accurately. For an electromagnetic pulse train with a nominal period T, the root mean square (RMS) deviation of $\{T_n - nT | n = 1, 2, \ldots\}$ is called timing jitter, where T_n is T_{COG} of the nth pulse. In this section, timing jitter measurements between different sources are discussed, including mode-locked laser pulses, microwave sources, and x-ray pulses.

A. Optical-to-Optical Timing

Based on Haus and Mecozzi's theoretical model [21], high-frequency timing jitter (e.g., >100 kHz) of passively mode-locked solid-state lasers can be much lower than 1 fs. In the past two decades, many approaches for reducing the measurement noise floor have been proposed to reveal the true timing jitter of mode-locked lasers. Initially, the timing jitter was characterized by the "direct detection method," where the laser output is first detected by a photodetector (PD), and then the phase noise is converted into an amplitude change by a mixer [22] for baseband power spectrum measurement. In this scheme, due to the photo-generated carriers, carrier scattering, energy-dependent space charge effects, and temperature variations, the generated electrical pulse after photodetection can be much noisier when compared to the original optical pulse. This noise, usually called amplitude-to-phase (AM-PM) noise conversion [23,24], limits the measurement precision to tens of femtoseconds. The balanced optical cross correlator (BOC) was then proposed to overcome this problem [25–28]. By directly converting the timing difference between two optical pulses into a voltage signal, this method is intrinsically immune to AM-PM noise.

Figure 1(a) shows the operation principle of a single-crystal BOC [27,28]. Two orthogonally polarized input pulses at 1550-nm center wavelength, and with an initial relative delay T_D, are focused into a type II phase-matched periodically poled $KTiOPO_4$ (PPKTP) crystal. The sum-frequency generation (SFG) component is transmitted through a dichroic mirror and detected by the first photodiode of the balanced PD (BPD). The input pulses at the fundamental harmonic are reflected by the dichroic mirror and again focused back into the PPKTP crystal. The SFG component generated during the backwards propagation is separated from the fundamental components by a dichroic beam splitter and detected by the second photodiode of the BPD. Because of the overlapping time

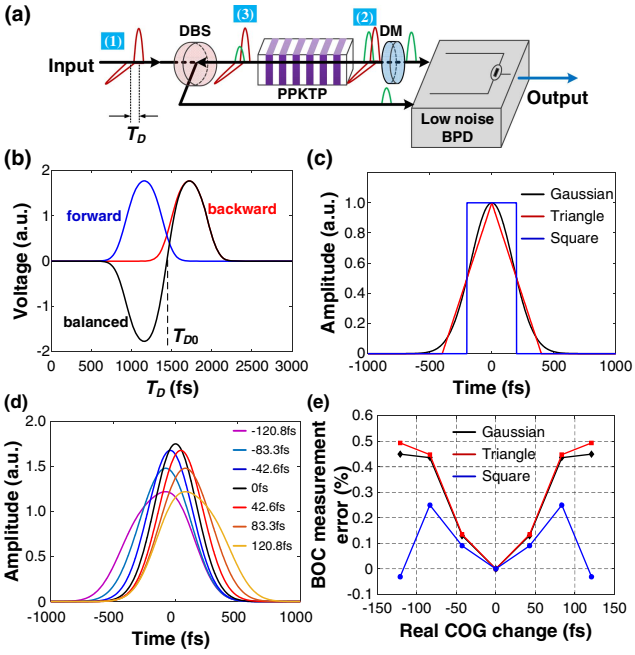

Fig. 1. (a) Operation of a single-crystal BOC (DBS, dichroic beam splitter; DM, dichroic mirror; PPKTP, periodically poled $KTiOPO_4$; BPD, balanced PD); (b) typical BOC characterization curve (T_{D0}, zero-crossing time). Analysis of different input pulse profiles: (c) Three types of input pulse E_1; (d) seven types of input pulse E_2, $E_2 = \exp[-(t/\tau)^2] + 0.75 \times \exp\{-[(t - t_d)/\tau]^2\}$, $\tau = 240.2$ fs, $t_d = 0, \pm 100$ fs, ± 200 fs, ± 300 fs; (e) calculated BOC measurement error for different COG change of E_2 ($L_c = 4$ cm, $k_1 = 1.386 \times 10^{-10}$ s/m, $k_2 = -1.569 \times 10^{-10}$ s/m).

difference in the crystal for different initial delays T_D, different voltage signals are obtained at the two photodiodes. For example, the blue and red curves in Fig. 1(b) show the detected voltage of the forward and backward SFG with different initial delay, and the black curve is the balanced output voltage, which can eliminate common background noise and provide a large timing sensitivity around the zero-crossing time T_{D0}.

The SFG process in Fig. 1(a) in undepleted fundamental-frequency approximation is governed by the coupled-wave equations [29]:

$$\left[\frac{\partial}{\partial z} + \left(\frac{1}{v_1} - \frac{1}{v_3}\right)\frac{\partial}{\partial t}\right] E_1 = 0, \tag{2}$$

$$\left[\frac{\partial}{\partial z} + \left(\frac{1}{v_2} - \frac{1}{v_3}\right)\frac{\partial}{\partial t}\right] E_2 = 0, \tag{3}$$

$$\frac{\partial}{\partial z} E_3 = i\frac{d_{\mathrm{eff}}\omega_3}{n_3 c} E_1 E_2, \tag{4}$$

where E_1, E_2, and E_3 are the electric fields of the two input pulses and SFG pulse, respectively, in the retarded time frame of E_3, with v_i denoting the group velocities of $E_i (i = 1, 2, 3)$. d_{eff} is the nonlinear optical coefficient, ω_3 is the carrier angular frequency of E_3, n_3 is the refractive index of E_3 in the crystal, and c is the vacuum speed of light. Based on Eqs. (2)–(4), the forward and backward SFG field can be obtained:

$$E_3^F(t, T_D) = K \int_0^{L_c} E_1(t - k_1 z) E_2(t - k_2 z - T_D) \mathrm{d}z, \quad (5)$$

$$E_3^B(t, T_D) = K \int_{L_c}^{2L_c} E_1(t - k_1 z) E_2(t - k_2 z - T_D) \mathrm{d}z, \quad (6)$$

where $K = i\omega_3 d_{\mathrm{eff}}/(n_3 c)$, $k_1 = 1/v_1 - 1/v_3$, $k_2 = 1/v_2 - 1/v_3$, and L_c is the crystal length. Then the BOC output voltage is given by

$$V_{\mathrm{BOC}}(T_D) \propto \int_{-\infty}^{+\infty} |E_3^F(t, T_D)|^2 \mathrm{d}t - \int_{-\infty}^{+\infty} |E_3^B(t, T_D)|^2 \mathrm{d}t. \quad (7)$$

At the zero-crossing time delay T_{D0}, we have $V_{\mathrm{BOC}}(T_{D0}) = 0$. Based on Eq. (1), there are two ways to change the T_{COG} of a pulse $E(t)$: either by introducing a delay to the whole pulse or by altering the temporal profile of $E(t)$. For the first case, if we introduce a delay Δt to the input pulse E_2, using Eqs. (1) and (5)–(7), it is straightforward to find out that both the T_{COG} of E_2 and T_{D0} of BOC will change by Δt, i.e., BOC can exactly measure this delay effect. For the second case, we choose seven different temporal profiles for E_2, which are obtained by adding two Gaussian pulses with different relative delays, as shown in Fig. 1(d). The calculated T_{COG} for each time profile is also given in the legend of Fig. 1(d). We use three different temporal shapes [Gaussian, triangle and square; see Fig. 1(c)] for E_1, and calculate the T_{D0} change (relative to the case when T_{COG} of E_2 is 0) for each different temporal profile of E_2. In Fig. 1(e), the T_{D0} variations measured by the BOC are compared with the real T_{COG} of E_2, and the maximum relative error is only 0.5%. This simulation proves that the BOC is a highly reliable optical-optical timing detector, as it can accurately measure the T_{COG} change of input pulses introduced by both a simple delay and a change in the temporal profile.

Figure 2 shows a typical setup for laser jitter characterization and synchronization based on a BOC. The output of two identical lasers (master and slave) are combined by a polarization beam splitter (PBS) and launched into a BOC. The BOC output was fed back to the slave laser's piezoelectric transducer (PZT) through a proportional-integral (PI) controller so that the two lasers' repetition rates are locked to each other. The real application of this setup is mainly determined by the locking bandwidth and gain of the PI controller. If the locking is very loose, the two lasers' timing jitter outside of the locking bandwidth will be present at the BOC output as voltage signals, which can be analyzed by an electrical spectrum analyzer, while if the locking is very tight, most of the timing jitter of the slave laser will follow that of the master laser; hence, a local timing synchronization between the two lasers is realized. Using a setup similar to that in Fig. 2, the timing jitter of erbium mode-locked fiber lasers was characterized by a

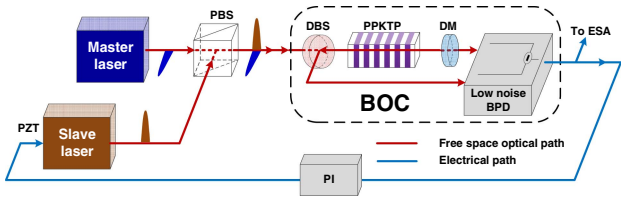

Fig. 2. Typical setup for laser jitter characterization and laser synchronization based on BOC (PBS, polarization beam splitter; PI, proportional-integral controller; ESA, electrical spectrum analyzer).

PPKTP-based BOC [30,31], with noise floors down to 10^{-12} fs^2/Hz for offset frequencies up to the Nyquist frequency of the laser.

Besides PPKTP, a BOC can also be realized with other nonlinear crystals, such as barium borate (BBO). By choosing proper phase-matching angles and crystal lengths, BBO can be optimized for SFG at different wavelengths. Therefore, different color BOCs can be made for various applications, such as single-color BOC for timing jitter characterization of Yb-fiber laser [32] and Ti:sapphire laser [33], two-color BOC for timing synchronization between a Ti:sapphire laser and a 1550-nm mode-locked laser [34,35], and Raman soliton timing jitter characterization at 1200–1300 nm [36].

All the BOCs discussed above are based on free-space optics. The timing sensitivities of these BOCs are limited by the low SFG efficiency in the bulk nonlinear crystals. In contrast, using integrated optics, since the optical beams can be confined in a small cross section during a long travel distance, the SFG conversion efficiency can be significantly increased. For example, a 90-fold improvement in aggregate conversion efficiency from a PPKTP waveguide was achieved over its free-space counterpart [37]. Using this technique, an integrated waveguide BOC was demonstrated at 1550 nm [38,39] with 10 times higher timing sensitivity, compared with free-space BOCs at the same input power level.

In general, the timing resolution of a BOC is limited by its noise floor, which is mainly due to shot noise and electronic detector noise. The shot noise-limited timing jitter spectral density $S_{T,\mathrm{shot}}^2$ is originated from the photon number fluctuation of the generated SFG signal, and can be calculated by

$$S_{T,\mathrm{shot}}^2 = 2eR_p P_{\mathrm{SFG}} G^2 / V_s^2, \quad (8)$$

where e is the electron charge, R_p is the detector responsivity, G is the detector transimpedance gain, P_{SFG} is the generated SFG power, and V_s is the timing sensitivity of the BOC. The electronic noise-limited timing spectral density $S_{T,\mathrm{electronic}}^2$ is decided by the detector's noise equivalent power (NEP):

$$S_{T,\mathrm{electronic}}^2 = (\mathrm{NEP} \cdot R_p G / V_s)^2. \quad (9)$$

Then the total timing noise spectral density S_T^2 is the sum of these two sources:

$$S_T^2 = S_{T,\mathrm{shot}}^2 + S_{T,\mathrm{electronic}}^2. \quad (10)$$

Figure 3 shows the calculated noise floor of BOCs with typical experimentally determined parameters at different input optical power levels. For both free space (blue) and integrated BOC (red), the noise floor is dominated by electronic noise at low input power and by shot noise at high input power. Due to the higher SFG efficiency, the integrated BOC's noise floor is 10–20 dB lower.

By increasing the input power level, the BOC's timing resolution can be continuously increased until it reaches the quantum limit of the input pulse itself. Based on Ref. [40], the photon distribution in optical pulses can lead the standard quantum limit of the timing jitter in a pulse train:

$$\langle \hat{T}^2 \rangle \geq \frac{\tau_{\mathrm{FWHM}}^2}{N}, \quad (11)$$

where τ_{FWHM} is the FWHM pulse width, N is the averaged photon number of each pulse, and $\hat{T}$ is the quantum operator of the pulse temporal COG. At about 100 mW and 1 W input power

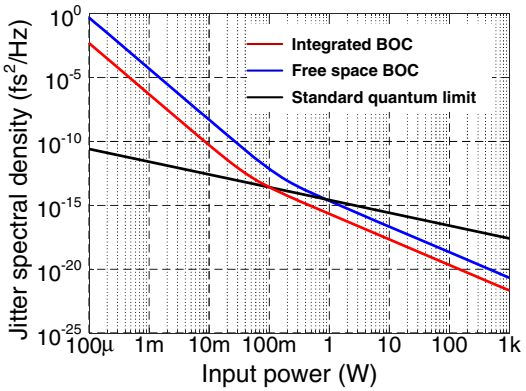

Fig. 3. BOC noise floors at different input average power levels. Pulse width, 100 fs; Nyquist bandwidth, 100 MHz; SFG efficiency, 4×10^{-2} W^{-1} (integrated), 4×10^{-3} W^{-1} (free space); BOC sensitivity for 200 mW (100 mW for each polarization) input power, 60 mV/fs (integrated), 6 mV/fs (free space); BPD responsivity, 0.6 A/W; BPD transimpedance gain, 1×10^3 V/A; BPD NEP, 7 pW/Hz$^{1/2}$.

level, respectively, the integrated and the free-space BOC will be limited by this standard quantum limit (black curve in Fig. 3).

As an alternative to the BOC, the timing jitter of mode-locked lasers can also be measured by a linear optical timing detection method based on optical heterodyning [41–43]. The concept is shown in Fig. 4. The repetition rates of two mode-locked lasers have a small difference of Δf_R. Two radio-frequency (RF) beats ("Beat 1" and "Beat 2") are formed between these two lasers by pair-wise interfering their long and short wavelength tails. By mixing these two heterodyne beat notes in a passive, doubled-balanced mixer at quadrature, a highly sensitive phase discrimination signal, which only depends on Δf_R, is generated. The two lasers are loosely locked with this phase-discrimination signal, and the free-running timing jitter at frequencies outside of the loop bandwidth can be measured with an RF spectrum analyzer.

In Ref. [43], a similar optical heterodyne technique is realized with the help of fiber delay lines. The long and short wavelength tails of a mode-locked laser are interfering with their delayed copies, and the common carrier frequency offset components are rejected by mixing the two heterodyne beat notes after PDs. Using this method, the timing jitter of a mode-locked laser can be directly characterized by itself without using another reference laser.

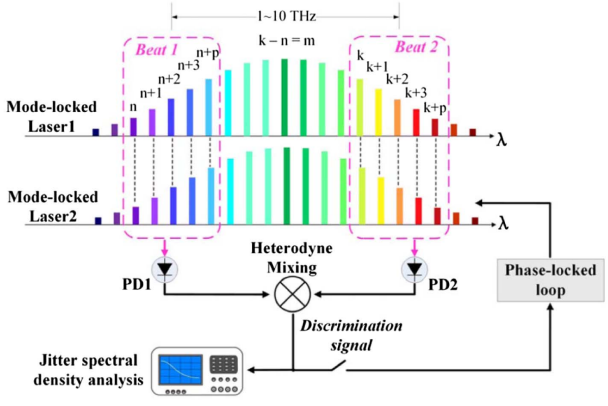

Fig. 4. Timing jitter measurement using an optical heterodyne technique. Figure adapted from Ref. [42].

A jitter noise floor of 2.8×10^{-13} fs^2/Hz (with 80 mW input power) and 2×10^{-9} fs^2/Hz (with 400 μW input power) was achieved in Ref. [42] and [43], respectively. In comparison with the BOC, this linear detection scheme can reach a smaller noise floor at low input power levels, while the noise floor will decrease more slowly with increasing input power (e.g., in the shot-noise-limited region, the BOC noise floor decreases 20 dB/decade, while in the case of linear detection, it drops only 10 dB/decade).

B. Optical-to-Microwave Timing

For a single-frequency microwave signal, we cannot use Eq. (1) to define its timing information. Alternatively, we use its phase noise to characterize the timing stability. Then, the equivalent timing jitter is given as

$$\Delta t_{\mathrm{RMS}}(f_1, f_2) = \frac{1}{2\pi f_c}\sqrt{\int_{f_1}^{f_2} S_\varphi(f)\mathrm{d}f}, \tag{12}$$

where $S_\varphi(f)$ is the single-sided spectral density of the signal's phase deviation, $[f_1, f_2]$ is the frequency range of interest, and f_c is the carrier frequency of the microwave signal. Conventionally, the phase noise of a microwave signal can be measured by mixing it with another microwave standard and then analyzing the resulting baseband signal. However, the timing sensitivity of this method is severely limited by the long period of the microwave signal (e.g., 1 fs equivalent timing jitter will only cause $2\pi \times 10^{-6}$ rad change for a 1 GHz signal). On the other hand, since mode-locked lasers can provide an ultrashort pulse train with ultralow timing jitter, such an "optically assisted" phase detection can provide much higher resolution for microwave phase discrimination. In the past decades, several kinds of optical-microwave phase detectors have been demonstrated [44–52].

Figure 5 shows the architecture of a free-space-coupled balanced optical-microwave phase detector (BOMPD), which was first proposed in Refs. [44,45] and improved in Refs. [46,47]. An optical pulse train with a repetition rate f_R from a mode-locked laser is launched into the device through the optical input port. The optical power is then separated into three paths: signal, bias, and reference, with free-space components, such as PBS, half-wave plates, and quarter-wave plates, which can efficiently reduce long-term drifts caused by the environment. Each path contains a free-space delay stage that enables precise phase tuning

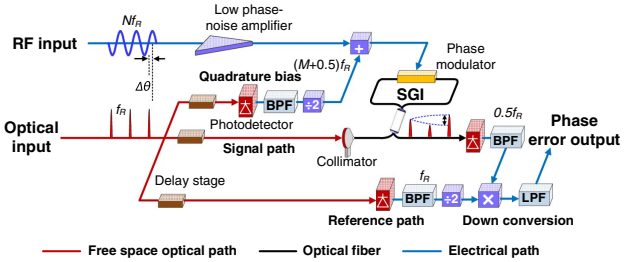

Fig. 5. Architecture of free-space-coupled balanced optical-microwave phase detector (f_R, the repetition rate of the optical input signal; $\Delta\theta$, the relative phase difference between the RF and optical input signals; SGI, Sagnac interferometer; BPF, bandpass filter; LPF, lowpass filter; ÷2, frequency divider; +, voltage summer; ×, frequency mixer). Figure adapted from [47].

without backlash, microwave reflection, and loss when compared with conventional RF phase shifters. In the signal path, the optical signal is coupled into a Sagnac interferometer (SGI) through a collimator. Since the temporal pulse width is sufficiently short, the optical pulse train power at the SGI input can be approximated by

$$P_{\text{in}}(t) = P_a T_R \sum_{n=-\infty}^{\infty} (1 + \Delta_{\text{RIN}}(t))\delta(t - nT_R - \Delta_J(t)), \quad (13)$$

where $\delta(t)$ is a Dirac delta function, $T_R = 1/f_R$ is the period of the pulse train, P_a, $\Delta_{\text{RIN}}(t)$, and $\Delta J(t)$ are the average power, power fluctuations, and timing jitter of the pulse train, respectively.

In the bias path, a self-referenced signal $(M + 0.5)f_R$ is derived from the optical pulse train after a PD, bandpass filter (BPF), and a frequency divider. Then the bias signal is sent to the phase modulator of the SGI together with the RF input signal at frequency $f_0 \approx N f_R$. Usually M is a very large number. Therefore, the multi-GHz modulation in the phase modulator ensures a unidirectional phase modulation, which eliminates the repetition-rate dependence of the SGI, thus improving its robustness and long-term stability when compared to earlier implementations [44,45]. The driving signal of the phase modulator can be written as

$$V_\varphi(t) = V_0 \sin[2\pi f_0(t + \Delta t_0)] + V_b \sin[2\pi(M + 0.5)f_R(t + \Delta t_b) + \Delta\phi], \quad (14)$$

where V_0 and Δt_0 are the amplitude and timing jitter of the RF input signal, respectively. V_b is the amplitude of the RF signal from the bias path. $\Delta\phi$ and Δt_b are the fixed relative phase and relative timing jitter between the pulse train and the RF bias signal, respectively. For biasing at quadrature, we have

$$V_b \sin(\Delta\phi) = V_\pi/2, \quad (15)$$

where V_π is the half-wave voltage of the phase modulator. Suppose the frequencies of the RF and optical input signals are locked with each other by the BOMPD, then $f_0 = N f_R$. Using Eqs. (13)–(15), the output optical power after circulating in the SGI can be expressed as

$$\begin{aligned} P(t) &= (1-\alpha)P_{\text{in}}(t)\sin^2\left(\frac{\pi V_\varphi}{2V_\pi}\right) \\ &= \frac{1-\alpha}{2}P_a T_R \sum_{n=-\infty}^{\infty}\left[1 + \frac{\pi}{V_\pi}V_b\left(-\frac{\theta_b^2}{2}\sin\Delta\phi + \theta_b\cos\Delta\phi\right)\right] \\ &\quad \times (1 + \Delta_{\text{RIN}})\delta(t - nT_R) \\ &\quad + \frac{1-\alpha}{2}P_a T_R \sum_{n=-\infty}^{\infty}\frac{\pi}{V_\pi}V_0\theta_e(1 + \Delta_{\text{RIN}})\delta(t - nT_R)e^{j\pi f_R t}, \end{aligned} \quad (16)$$

where α is the loss of the SGI, $\theta_e = 2\pi f_0(\Delta t_0 + \Delta J)$ is the relative phase error between the pulse train in SGI and RF input signals, and $\theta_b = 2\pi(M + 0.5)f_R\Delta t_b$ is the phase fluctuation in the bias path.

The SGI output is filtered by a BPF at $0.5f_R$ to perform the frequency downconversion with the signal in the reference path. Since the $0.5f_R$ frequency component only appears in the second term on the right-hand side of Eq. (16), the phase fluctuations θ_b from the bias path cannot affect this downconversion process. Finally, the error signal after downconversion is

$$V_e = \frac{C}{2}\frac{\pi}{V_\pi}(1-\alpha)P_a T_R V_{rp} V_0 \theta_e (1 + \Delta_{\text{RIN}})\cos(\pi f_R \Delta t_r), \quad (17)$$

where V_{rp} is the amplitude of the RF signal in the reference path, Δt_r is the relative timing jitter between the reference and the SGI path, and C is a constant coefficient related to the downconversion electronics. Since the downconversion is performed at the lowest possible frequency ($0.5f_R$), thermally induced phase changes in the reference path can be minimized. For example, if $f_R = 216$ MHz, a 3-mm length change from the reference path can only introduce 2×10^{-5} relative change to V_e. Similarly, since usually $\Delta_{\text{RIN}} \ll 1$, V_e is also insensitive to optical input power fluctuations. Thus, V_e is mainly determined by θ_e, i.e., the relative timing jitter between the RF and SGI input signals. Since the free-space optical paths before the SGI are well isolated from environmental changes, the BOMPD can accurately detect the timing jitter between the RF and optical input signals without introducing systematic errors.

The quadrature bias condition in Eq. (15) can also be realized with different methods. In Refs. [48,49], a nonreciprocal quarter-wave bias unit with two Faraday rotators and a quarter-wave plate is employed in the fiber loop (Fig. 6). Then the polarizations of counterpropagating pulses are aligned to the slow and fast axis of the quarter-wave plate, respectively. Therefore, a $\pi/2$ phase bias is obtained automatically. In Ref. [50], the optical pulse train is sent into a dual-output Mach–Zehnder modulator, and the $\pi/2$ phase bias is achieved by imposing a DC offset voltage on one arm of the modulator. In Ref. [51], a simple 3×3 fiber coupler structure is introduced, so the $\pi/2$ phase bias condition is automatically maintained for a Sagnac loop. In all these schemes, the phase error signal is encoded in the mode-locked laser's baseband power change; thus, a balanced detection is necessary to remove the laser's high average power. Special attention must be paid to suppress the AM-PM noise conversion, as discussed in Ref. [52].

Besides optical-microwave phase detectors, significant progress has also been made in converting precision timing information from optical domain to microwave domain through direct photodetection. In Ref. [53], modified unitraveling carrier PDs are introduced to provide a null of the AM-PM conversion at a specific bias voltage. By using an optical-microwave interferometer setup, the measured excess timing noise in the photodetection is 4 as/$\sqrt{\text{Hz}}$ at 1-Hz offset. In Ref. [54], a digital coherent modulation-demodulation system is used to actively stabilize the PD so as to make it operate continuously in a null of the AM-PM conversion state.

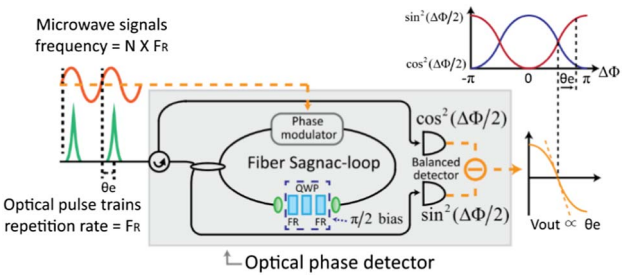

Fig. 6. Fiber-loop optical-microwave phase detector (FLOMPD). Figure adapted from [48].

C. X-Ray Pulse Timing

The general timing jitter definition in Eq. (1) also applies to an x-ray pulse. To fully characterize its jitter, we need to know the x-ray pulse profile, as well as its delay relative to another reference signal (electron bunch, optical pulse, etc.). The timing jitter characterization of XFEL x-ray pulses has attracted wide interest in the past decade, since it is crucial to realize the longstanding dream of recording a molecular movie. Here, we discuss a few prominent techniques related to XFEL x-ray timing.

First, without any external source, an XFEL pulse can be characterized by cross-correlation between itself and its original electron bunch [55]. In Ref. [55], an emittance-spoiling foil with double slots is used in the LCLS, the hard x-ray FEL in Stanford, U.S. After the electron beam passes through the foil, only the two unspoiled time slices with good emittance can contribute to the FEL lasing. So, a femtosecond x-ray pulse pair is generated. A magnetic chicane is added in the middle of the FEL undulator. It plays two roles: to wash out the FEL microbunching generated in the first part of the undulator, and to delay the electron beam with respect to the x-ray pulses. From the cross-correlation trace between the chicane-induced delay and the detected x-ray pulse intensity, both the pulse separation of the pair and the pulse duration of each pulse can be extracted. The measurement resolution obtained with this method is sub-10 fs [55].

The arrival time of XFEL pulses relative to external probe laser pulses can be indirectly determined using a noninvasive technique based on electro-optic sampling (EOS) of the electric field surrounding the ultrarelativistic electron bunch that produces the x-ray pulse [56]. As shown in Fig. 7, if a crystal is placed adjacent to the electron beam, its index of refraction will be distorted anisotropically by the strong electromagnetic fields associated with the ultrarelativistic electrons. This transient birefringence or electro-optic effect is induced without affecting the electron bunch propagation. Laser light passing through the crystal at the same time as the transient birefringence will have its polarization rotated and can be used to probe this effect. In the limit that the crystal response is electronic, this transient birefringence is prompt, and the effect is proportional to the electron bunch current profile. With this method, a resolution better than 60 fs RMS can be achieved for x-ray pulse relative timing measurements.

The method in Ref. [56] can only detect the relative timing between the electron bunch and the optical laser pulse. The additional timing jitter between the electron bunch and the generated x-ray pulse cannot be resolved. Later, an improved scheme was proposed [57]. This time, the EOS is performed with the coherent terahertz radiation generated at the end of the x-ray undulator by the same electron bunch that emits the x-ray pulse. These terahertz electric fields and the x-ray pulses are intrinsically synchronized to one another on the scale of a few femtoseconds. Therefore, if the optical pulse is synchronized with the terahertz electric field using the EOS, it is also synchronized to the x-ray pulse, within a few femtoseconds' temporal resolution.

Induced ultrafast optical switching of bulk refractive indices is another common cross-correlation technique to resolve the timing jitter of vacuum ultraviolet or x-ray pulses. Absorption of a fraction of the x-ray beam intensity can produce a rapid change in the free-carrier density by photoionization and subsequent cascade ionization. In Ref. [58], ultrafast transient changes of the optical reflectivity in GaAs induced by femtosecond x-ray excitation is used to directly measure the timing between x-ray and optical pulses. Extreme UV radiation pulses with a duration of 50 fs impinge on a GaAs(100) crystal with the electric-field vector in the surface plane. The induced change of optical reflectivity is probed by a delayed optical pulse at 800 nm, or optionally, 400 nm, with a FWHM duration of 120–150 fs delivered from an optical parametric amplifier system that is electronically synchronized to the electron accelerator. The optical pulse energies are detected in a reference path, and after reflection with two fast photodiodes, allow for transient reflectivity measurements pulse by pulse. Based on the detected x-ray-induced optical reflectivity, the initial delay between the optical and x-ray pulse can be obtained, and the relative timing jitter of the x-ray pulses can also be compensated. A similar method is used in Ref. [59] to measure the relative timing jitter between hard x-ray pulses and optical pulses. The hard x-ray pulses are sent through 1 μm Si_3N_4 membranes. Such thin membranes ensure x-ray transmission higher than 90% and are not damaged by the FEL pulses. The x-ray-induced transmission change can then be probed by an optical pulse. The relative delay is either encoded in wavelength from a broadband chirped supercontinuum of the optical pulse, or encoded in the spatial domain by providing a grazing angle to the FEL pulse. The final optical-x-ray delay measurement error is 6 fs RMS.

Finally, terahertz streaking [60,61] constitutes another technique for x-ray pulse characterization. As illustrated in Fig. 8, blue and red curves represent the electric field and the corresponding

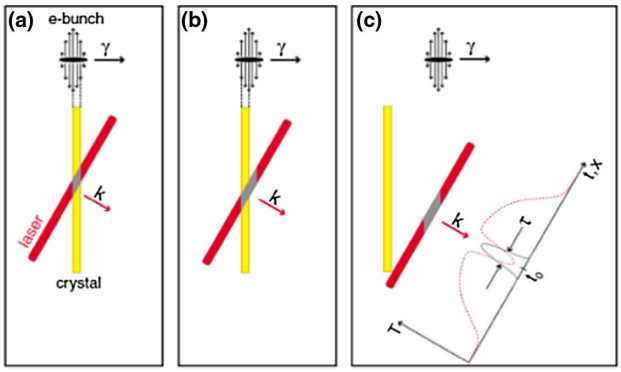

Fig. 7. X-ray pulse timing measurement based on EOS. Reprinted with permission from American Physical Society [56], ©2005.

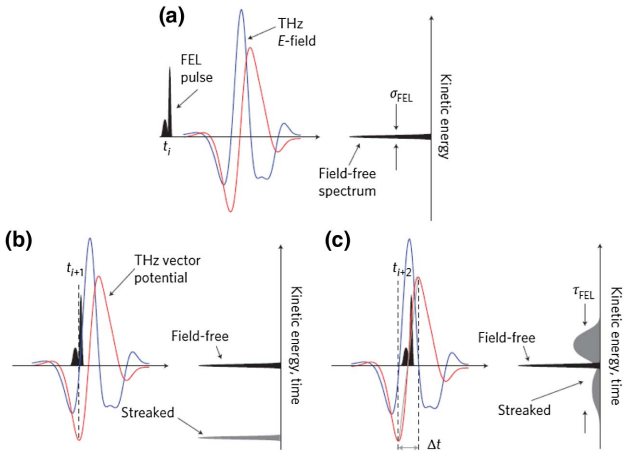

Fig. 8. Schematic of single-shot, single-cycle terahertz streaking measurement. Reprinted with permission from Springer Nature [60], ©2012.

vector potential of a single-cycle terahertz pulse. The vertical axis gives the kinetic energy of the photoelectron emission, which is equivalent to time in streaking measurements. During the single-shot measurement shown in Fig. 8(a), the FEL pulse does not overlap in time with the terahertz pulse, and the kinetic energy distribution of the photoelectrons ejected by the FEL pulse is unaffected. In Fig. 8(b), the FEL pulse overlaps with an extreme of the terahertz vector potential, leading to a maximally downshifted photoelectron spectrum with minimized spectral broadening. In Fig. 8(c), the temporal overlap occurs near the zero crossing of the terahertz vector potential, where the time of arrival as well as the temporal profile and duration can be accessed with the highest resolution. In Ref. [60], the single-cycle terahertz pulses generated by optical rectification of femtosecond Ti:sapphire laser pulses has a streaking field half-cycle or ramp of ~600 fs, significantly longer than the maximum expected FEL pulse duration and timing jitter. As a result, once the streaking pulse and FEL pulse are overlapped temporally, all single-shot acquisitions occur on a uniquely defined, nearly linear portion of the streaking ramp. The terahertz electric field is characterized by the EOS independently to construct the streaking map. Since the terahertz electric field is locked to the Ti:sapphire laser, the resulting FEL pulse profile measurements are given on a time base that is synchronized to the pump-probe experiment environment. The achieved temporal profile measurement accuracy of individual FEL pulses is 5 fs FWHM.

3. FREE-SPACE-BASED LARGE-SCALE TIMING SYSTEM

Generally, a timing and synchronization system consists of a timing reference providing extremely stable timing signals, a target signal that needs to be synchronized, a timing detector that can measure the timing difference between the target signal and the reference, and a control system to lock the timing of the target to that of the reference. Using the timing characterization tools presented in Section 2, we can locally synchronize the timing of different kinds of signals. If the target device is located far away from the reference, a timing link is necessary to deliver the timing signal from the reference to the target. Timing links can be constructed through either free-space or optical fibers. In this section, we first discuss the free-space case.

In many large-scale scientific instruments, such as XFELs and ELI facilities, high-power ultrashort pulse optical lasers are generated from a laser chain that typically consists of a seed oscillator, multistage amplification, regenerative amplifier cavities, active elements, as well as tens of meters of propagation length. All these components make the system prone to long-term timing drift and fast jitter sources. Optical synchronization of the final amplifier output to the seed oscillator is required in many applications such as pump-probe experiments and pulse synthesis [62–66]. In Ref. [63], a timing correction is demonstrated for a terawatt scale Ti:sapphire laser system at Swiss FEL, operating at 5 Hz. The timing difference between the final output pulse and the seed oscillator is compared by a BOC with a single-pass type I BBO crystal. Due to the large beam diameter of the final pulse output, the two beams in the BBO crystal are noncollinearly mixed, and therefore the generated SFG signal can be spatially separated from the inputs. The reference input pulse is stretched by a CaF_2 block to apply a well-defined chirp; therefore, the relative timing can be translated to a wavelength change of the SFG signal, which appears as a spatial displacement after a UV grating and is measured by a CCD camera. Due to the low operating frequency (5 Hz), the timing correction is implemented every shot by controlling a motor stage based on the BOC output. The achieved timing precision is ~3 fs RMS for several hours.

Regenerative amplifiers are most often used to deliver multi-millijoule output pulse energies for terahertz generation, high-harmonics generation, optical parametric amplifiers, etc. The inherent principle of regenerative amplifiers implies a pulse buildup time on the order of a few microseconds, which is equivalent to an optical path length of hundreds of meters. Thus, the regenerative amplification architecture is potentially sensitive to external perturbations such as mechanical vibrations, temperature fluctuations, and pressure variations. Figure 9 shows a typical timing stabilization scheme for regenerative amplifiers [64]. The BOC for timing detection between the seed oscillator and the regenerative amplifier is realized by two lithium triborate (LBO) crystals. This approach is also based on a noncollinear SFG configuration due to the amplifier large beam diameter. Two glass plates are placed in the regenerative amplifier arm before one LBO, to obtain an S curve from BOC output. Here, the optical delay line for timing compensation must be able to support a large feedback bandwidth, so that the timing jitter up to the Nyquist frequency of the regenerative amplifier repetition rate can be corrected.

Large-scale free-space frequency comb transfer has been demonstrated in both indoor and outdoor environments, where the system bears atmospheric turbulence. In Ref. [67], by using BOC to characterize and suppress atmospheric timing fluctuation, one-way transfer of an optical pulse train is realized over a 76.2-m-long free-space beam path in a laboratory environment, with 2.6 fs residual jitter over 130 h. Another one-way transfer scheme is presented in Ref. [68]. A frequency comb is transferred over a 52-m-long free-space outdoor link with passive phase conjunction correction. The frequency instability is reduced to 6×10^{-17} at 1000 s.

In Ref. [69], optical two-way time and frequency transfer over free space is demonstrated. As depicted in Fig. 10, two clocks are located at separate sites A and B. Suppose site A transmits a pulse from an optical comb at its zero time to site B. Its measured arrival time according to site B's clock is $\Delta\tau_{A\to B} = T_{\text{link}} + \Delta T_{AB}$, where T_{link} is the path delay and ΔT_{AB} is the time offset between the clocks. Simultaneously, site B transmits a pulse at its assumed zero time in the opposite direction to site A, where its arrival time is $\Delta\tau_{B\to A} = T_{\text{link}} - \Delta T_{AB}$. Subtraction of these two arrival times yields the clock time offset, $\Delta T_{AB} = (\Delta\tau_{A\to B} - \Delta\tau_{B\to A})/2$,

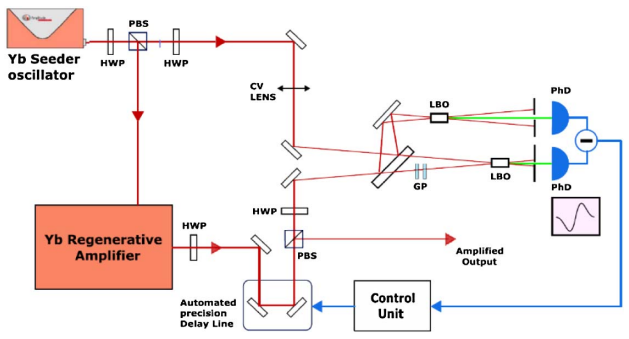

Fig. 9. Experimental setup for the characterization and stabilization of the regenerative amplifier repetition rate. Figure adapted from [64].

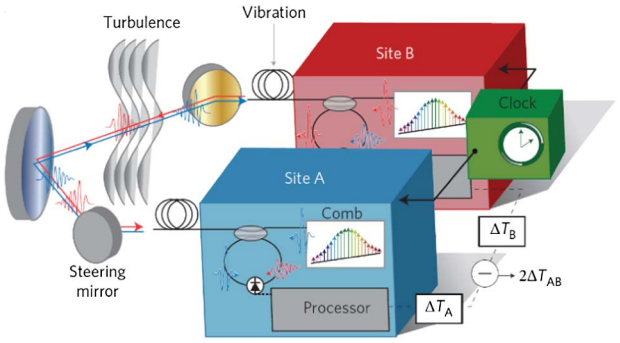

Fig. 10. Optical two-way time and frequency transfer over free-space link. Reprinted with permission from Springer Nature [69], ©2013.

which can be used to evaluate the cumulative relative timing error between these two clocks. $\Delta\tau_{A\to B}$ and $\Delta\tau_{B\to A}$ can be measured accurately by the BOC method [70]. Alternatively, linear optical sampling is adopted in Ref. [69]. In this scheme, the combs at two sites are phase-locked to the same optical clock, but with the repetition rates differing by Δf_R. At each site, the heterodyne detection between the transferred comb and the local comb yields an interferogram, or a cross correlation. From the peak location of the cross correlation, the relative timing between pulse trains can be inferred, with an update rate of Δf_R. Although T_{link} is canceled in the two-way transfer, it may still interrupt the measurement when the turbulence effect is too strong to fade the received signal below an accepted level. A steering mirror is used in Fig. 10 to compensate the turbulence-induced angle-of-arrival jitter. With all these techniques above, the measured timing difference ΔT_{AB} is 2.5 fs RMS (100 ms sampling time) within a few hours.

This optical two-way time transfer method is later used in remote synchronization among different kinds of sources over free-space links. In Ref. [71], two identical optical clock combs are independently locked to two optical cavities at the two sites. A third "transfer" comb is sent from the master site to a remote site for linear optical sampling over a turbulent 4-km free-space link. A coarse two-way time transfer between two pseudorandom binary sequence-modulated distributed feedback lasers is used to estimate T_{link} and other parameters, and then a more complicated equation is used to determine ΔT_{AB}, which serves as the timing error to synchronize the remote clock comb. The achieved time wander between two synchronized combs is 40 fs peak to peak, over a 2-day measurement. A similar experimental setup is also used to synchronize a microwave clock and an optical clock [72], and for two-way carrier-phase extraction [73]. In both Refs. [71,72], absolute time delay measurement can be performed with femtosecond precision.

4. FIBER-BASED LARGE-SCALE TIMING SYSTEM

Compared to free-space-based links, optical-fiber-based timing links are much more mechanically stable, flexible for installation, and can be easily fitted into telescopes and XFELs. Transferring cw lasers in fiber links has been widely used in frequency metrology [74–77]. Arbitrary fiber links at telecommunication wavelength can be utilized, since there are no dispersion or nonlinear effects for a cw source. Using the two-way exchange scheme, a fractional instability of 10^{-19} (35,000 s) is achieved for stabilizing two 920-km fiber links [77]. In order to extract timing information, additional optical combs, which can be locked to the transfer cw lasers, are required at each end station of the links. This makes this scheme not very practical for timing and synchronization. Another method is to transfer a microwave signal that is amplitude-modulated on a cw optical carrier [78,79]. The timing information is carried by the microwave signal. Dispersion and nonlinear effects in the link are negligible. Due to the low timing discrimination with microwaves and the high noise floor at photodetection, this scheme can only deliver ~100 – fs level timing jitter in remote synchronization systems. The last scheme is to transfer ultrafast optical pulses via fibers, which will be discussed in detail in this section. In the pulsed approach, an optical pulse train with ultralow jitter (timing signal) is generated from a mode-locked laser (master laser), and distributed through fiber links in a star network topology. Due to the broad bandwidth of the optical pulse, the fiber links need to be carefully designed to reduce dispersion, nonlinearity, and other undesired effects.

A. Fiber-Based Timing Link Stabilization

Figure 11 shows the fiber timing link stabilization scheme based on the optical pulse approach. This scheme was first proposed in Refs. [45,80] using a 300-m dispersion-compensated single-mode fiber (SMF) link. Due to the polarization mode dispersion (PMD), the residual timing jitter after link stabilization was limited to sub-10 fs level, and could escalate to as much as 100 fs when the fiber was significantly perturbed. The SMF link is later replaced by a 1.2-km polarization-maintaining dispersion-compensated fiber (PM-DCF) to eliminate the PMD effects [81]. The measured residual timing jitter is reduced to subfemtosecond level over a 16-day operation.

In Fig. 11, the link input signal is first divided into reference and link path pulses. The reference path length is set as short as possible (e.g., 4 cm) to minimize timing errors introduced by environmental noise. A fiber mirror is placed at the end of the link to reflect a portion of the link pulses back for stabilization. To assure that the forward and backward link transmission accumulates the same amount of jitter, the link pulse must travel along the same polarization axis during round-trip propagation. Therefore, a 45° Faraday rotator before the fiber link is necessary to introduce a 90° round-trip polarization rotation to direct the reflected link pulse toward the BOC. In the control module, the output voltage of a PI controller is divided into two paths. The first path compensates for fast noise in the link and usually consists of a high-voltage amplifier that drives a PM fiber stretcher. The second path compensates for long-term environmental drift;

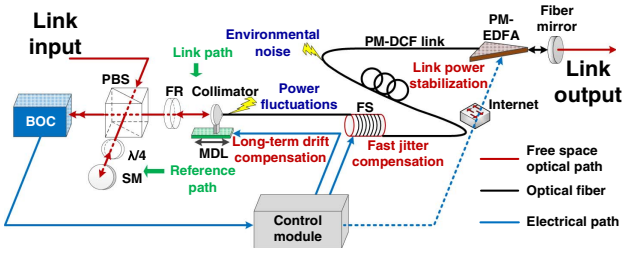

Fig. 11. Typical link stabilization setup (SM, silver mirror; $\lambda/4$, quarter-wave plate; FR, 45° Faraday rotator; MDL, motorized delay line; FS, fiber stretcher; PM-DCF link, polarization-maintaining dispersion-compensated fiber link; PM-EDFA, polarization-maintaining erbium-doped optical fiber amplifier). Figure adapted from [47].

a data acquisition card is usually used to sample the timing error, and control commands can be sent to a motorized delay line through a computer.

Using fiber-coupled integrated BOC [38], fiber-coupled PBS, fiber-coupled Faraday mirror, and fiber-coupled motorized delay line, an all-fiber-coupled timing link stabilization system is demonstrated in [82]. The robustness and ease of implementation of these fiber-coupled devices can eliminate alignment-related problems observed in free-space optics. However, since optical fiber is more sensitive to environmental temperature, the total residual timing drift (<1 Hz) was 3.3 fs RMS over 200 h of operation, even though PM-DCF fiber links were adopted. In Ref. [83], a new integrated BOC is employed [39] with improved timing sensitivity. Except for the fiber-coupled integrated BOC, all the other optics are realized in free space. The measured residual timing drift is reduced to 0.75 fs (<1 Hz) over 28 h. Due to the higher timing sensitivity, the main advantage of using integrated BOCs in timing link stabilization is on the power budget. With the same master laser, the integrated BOCs can support 3 times more links compared to free-space BOCs [83].

B. Fiber-Link-Induced Timing Jitter

In Fig. 11, long-range compensation is performed by a motorized stage with long free-space delay arms; e.g., a 10-cm range is required to correct for ±1.5-K temperature change in a 3.5-km link. Movement of the delay stage introduces inevitable beam misalignments that cause link power fluctuations. We can use an analytical model to investigate how these fluctuations affect the COG of the optical pulses.

In the retarded time frame of pulse propagation in the fiber link, we define $A(z, T)$ as the slowly varying amplitude of the link pulse envelope. $A(z, T)$ is governed by the nonlinear Schrödinger equation [84]:

$$\frac{\partial A}{\partial z} = \left(-\frac{\alpha}{2} - \frac{i\beta_2}{2}\frac{\partial^2}{\partial T^2} + \frac{\beta_3}{6}\frac{\partial^3}{\partial T^3}\right)A(z,T) + i\gamma\left(|A|^2A + \frac{i}{\omega_0}\frac{\partial}{\partial T}(|A|^2A) - T_R A\frac{\partial |A|^2}{\partial T}\right), \quad (18)$$

where α is the fiber loss, β_2 is the second-order dispersion (SOD) coefficient, β_3 is the third-order dispersion (TOD) coefficient, γ is the nonlinear parameter for self-phase modulation (SPM), ω_0 is the carrier angular frequency, and T_R is the Raman parameter. The timing link consists of two fiber sections: standard polarization-maintaining (PM) fiber and PM dispersion-compensating fiber (DCF). Here it is assumed that α and T_R are constants, and β_2, β_3, and γ are z-dependent.

The slowly varying amplitude of the pulse envelope can be written in terms of a normalized amplitude function U on a time scale t normalized to the input pulse width T_0 as

$$A(z, T) = \sqrt{P_0}\exp(-\alpha z/2)U(z, t), \quad (19)$$

where $t = T/T_0$, P_0 is the peak power of the input pulse. Substituting Eq. (19) into Eq. (18), $U(z, t)$ satisfies

$$U_z = -\frac{i\beta_2}{2T_0^2}U_{tt} + \frac{\beta_3}{6T_0^3}U_{ttt} + i\gamma P_0\exp(-\alpha z)\left(|U|^2U + \frac{i}{\omega_0 T_0}(|U|^2U)_t - \frac{T_R}{T_0}U|U|_t^2\right), \quad (20)$$

where the subscripts t and z indicate partial derivatives, e.g., $U_z \equiv \partial U/\partial z$, $U_{tt} \equiv \partial^2 U/\partial t^2$.

The COG of $A(z, T)$ can be written as

$$t_{\mathrm{COG}} = \frac{\int_{-\infty}^{+\infty} T|A(T)|^2\mathrm{d}T}{\int_{-\infty}^{+\infty}|A(T)|^2\mathrm{d}T} = T_0\int_{-\infty}^{+\infty} t|U(t)|^2\mathrm{d}t. \quad (21)$$

Based on Eqs. (20) and (21), we have

$$t_{\mathrm{COG}} = \frac{1}{2T_0^2}\int_{-\infty}^{+\infty}|U_t(t,0)|^2\mathrm{d}t\int_0^L\beta_3\mathrm{d}z - P_0\begin{bmatrix} 2\frac{T_R}{T_0^2}\int_0^L\beta_2\int_0^z\gamma\exp(-\alpha z_1)F_1(z_1)\mathrm{d}z_1\mathrm{d}z \\ +\frac{1}{T_0^2}\int_0^L\beta_3\int_0^z\gamma\exp(-\alpha z_1)F_2(z_1)\mathrm{d}z_1\mathrm{d}z \\ -\frac{T_R}{T_0^3}\int_0^L\beta_3\int_0^z\gamma\exp(-\alpha z_1)F_2(z_1)\mathrm{d}z_1\mathrm{d}z \\ +\frac{3}{2\omega_0}\int_0^L\gamma\exp(-\alpha z)S(z)\mathrm{d}z \end{bmatrix}, \quad (22)$$

where

$$F_1(z) = \int_{-\infty}^{+\infty}(|U|_t^2)^2\mathrm{d}t, \quad (23)$$

$$F_2(z) = \int_{-\infty}^{+\infty}|U|_t^2(UU_t^* - U^*U_t)\mathrm{d}t, \quad (24)$$

$$F_3(z) = \int_{-\infty}^{+\infty}|U|_{tt}^2(UU_t^* - U^*U_t)\mathrm{d}t. \quad (25)$$

Based on the second term in Eq. (22), it can be concluded that the change of t_{COG} induced by power fluctuations is proportional to the input power level and is a combined effect of residual SOD, TOD, SPM, self-steepening, and Raman response. Although a COG shift appears as a deterministic shift in the zero-crossing position of the BOC characteristic in Fig. 11, the link stabilization feedback will unknowingly track this shift and erroneously introduce it into the link path, causing a timing error at the link output.

Simulation results are given in Fig. 12 to quantify the link-induced timing drift effects [47]. SPM, self-steepening, and the Raman effect are considered in the link. The BOC characteristic is calculated for each round-trip link pulse against a new laser reference pulse. The timing offset of the zero-crossing position in the BOC characteristic is identified as timing error. The parameters B2/B3 are used to represent the link residual SOD/TOD normalized by the SOD/TOD of 1-m standard PM 1550 fiber. Figure 12(a) shows that residual TOD can induce up to 5-fs timing error for +8-dBm average power in the link (considering 200-fs input pulse width and 200-MHz repetition rate) with ±5% fluctuations. Figure 12(b) indicates that +10-dBm link power is the threshold before significant amplitude-to-timing conversion

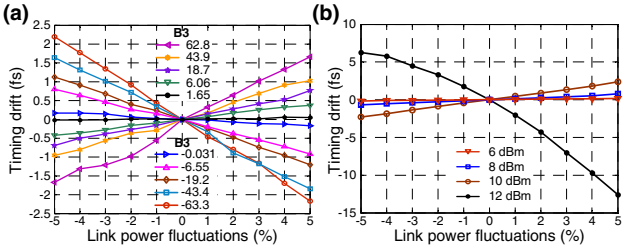

Fig. 12. Timing drift introduced by link power fluctuations [in (a), the input power is +8 dBm and B2 = –0.13; in (b), B2 = –0.13 and B3 = 18.7]. Figure adapted from [47].

occurs due to severe nonlinear pulse distortions that may result in 4 fs of timing error from ±5% power fluctuations. In order to eliminate these power-fluctuation-induced drifts, the link power must be stabilized. As shown in Fig. 11, this can be realized by sending a third feedback signal to the polarization-maintaining erbium-doped optical fiber amplifier (PM-EDFA) to adjust its pump current.

Besides the long-term drifts, the fast jitter of an optical pulse train can also be enhanced during fiber link transmission [47]. To investigate this effect, the master equation of a fast-saturable-absorber mode-locked laser is solved using the fourth-order Runge–Kutta in the interaction picture (RK4IP) method [85]. Laser timing jitter is generated by adding amplified spontaneous emission noise during each iteration of RK4IP. The calculation is repeated for a train of laser pulses in the presence of pulse timing jitter, and each pulse is solved by similar procedures in the link-induced drift simulation.

In Fig. 13(a), pulse center-frequency fluctuations are converted into timing jitter via residual SOD and TOD. This jitter contribution, often called Gordon–Haus jitter [86], can amount to 0.15 and 0.3 fs for uncompensated SOD equivalent to 2 and 3 m of standard PM fiber, respectively. In Fig. 13(b), spontaneous emission noise is converted into timing jitter, and its impact is further enhanced by link nonlinearities. The introduced jitter reaches up to 0.13 fs for average power levels below +12 dBm (corresponding to a pulse peak power of $P_{peak} = 430$ W) but escalates to 1.4 fs at +14 dBm ($P_{peak} = 682$ W). This jitter needs to be carefully minimized in practice because it easily reaches the femtosecond-level before a visible distortion of the BOC characteristic can be observed, as shown in the inset of Fig. 13(b).

C. Fiber-Based Remote Timing Synchronization

After stabilizing the fiber-based timing link, the pulsed timing signal can be used to remotely synchronize optical and microwave sources. In Ref. [87], two optical lasers are synchronized over a 3.5-km PM-DCF link using a BOC. The out-of-loop drift (<1 Hz) is 2.3 fs over 40 h of operation. It is mainly limited by the power-fluctuation-induced timing error given in Eq. (22) and Fig. 12. In Ref. [88], remote microwave synchronization is realized over a 2.3-km SMF link. The repetition rate of the master laser is first locked to a local RF reference by a fiber-loop optical-microwave phase detector (FLOMPD). The delivered timing signal from the master laser after link transmission is used to lock a remote voltage-controlled oscillator (VCO) by another FLOMPD. The demonstrated relative fractional frequency instability is 7.6×10^{-18} at 1000 s averaging time, which is limited by the PMD drifts of the fiber link.

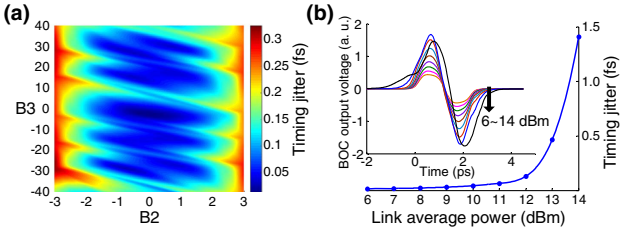

Fig. 13. (a) Link-induced Gordon–Haus timing jitter for different B2/B3 values; (b) link-induced timing jitter due to nonlinear effects in the fiber. Figure adapted from [47].

A laser-microwave network is demonstrated in Refs. [47,89], with the aim of minimizing all conceivable technical noise sources. As shown in Fig. 14, the repetition rate of the master laser is locked to a microwave reference with a 10-Hz feedback bandwidth to suppress long-term drifts. The timing signal from the master laser is distributed through a network that contains two independent fiber links of 1.2-km and 3.5-km length operated in parallel. The link outputs are used to synchronize a remote laser and a VCO simultaneously. The residual SOD and TOD of the links are compensated with additional DCF to suppress the link-induced Gordon–Haus jitter [Fig. 13(a)] and to minimize the output pulse durations for high signal-to-noise ratio (SNR) in the BOCs. The link power is adjusted to minimize the nonlinearity-induced jitter [Fig. 13(b)] as well as to maximize the SNR for BOC locking. To eliminate power-fluctuation-induced drift (Fig. 12), a feedback signal was sent to the EDFA to control its pump current. A free-space-coupled-BOMPD is employed for optical-microwave locking to improve the long-term timing stability. The relative timing instability of remote laser synchronization was 9×10^{-22} in 10^5 s. The relative timing jitter between the two remote-synchronized devices over the full measurement frequency range [15 μHz, 1 MHz] was 950 as RMS.

Using the same 4.7-km timing link network in Fig. 14, a multicolor laser network with daily 0.6-fs timing drift is demonstrated using two-color BOCs [90]. A microwave network is also realized with a total residual phase error of 147 μrad at 10 GHz integrated from 0.1 mHz to 100 MHz [91,92].

In summary, Fig. 15 shows a typical timing and synchronization system for an XFEL. It can be implemented using the techniques discussed in this paper. For example, timing link

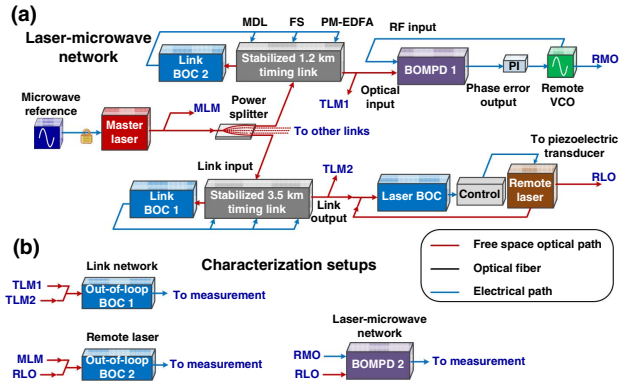

Fig. 14. (a) Laser-microwave network; (b) out-of-loop characterization setups. Figure adapted from [47].

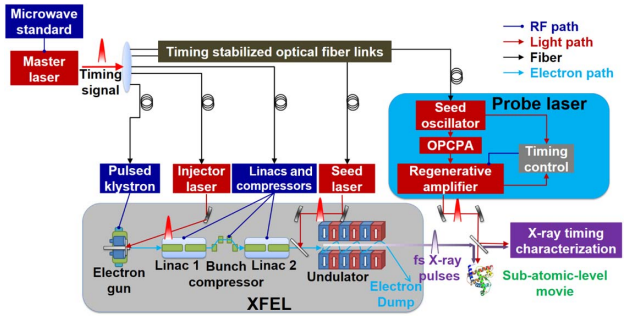

Fig. 15. Timing synchronization of XFEL.

stabilization by [47,61,81–83], the synchronization between the microwave reference and master laser, master laser to klystron, linear accelerators, and bunch compressor by [44–52,61,88,91,92], master laser to injector laser, seed laser and seed oscillator of the probe laser by [34,35,38,39,47,61,87,90], probe laser seed oscillator to probe laser output by [62–66], and x-ray timing characterization by [58–61].

D. Quantum Limit of Fiber-Based Timing System

Before concluding this section, we use a semiclassical model in the Heisenberg picture to investigate the quantum limit for the timing jitter of the fiber-based timing link. The quantized optical electric field in the fiber can be written as [93]

$$\hat{E}(t) = i\int_0^\infty \mathrm{d}\omega\left(\frac{\hbar(\omega+\omega_0)\eta}{4\pi\varepsilon_0 c|n|^2 S}\right)^{1/2}\hat{c}(\omega+\omega_0)e^{-i(\omega+\omega_0)t}, \tag{26}$$

where ω_0 is the field center frequency, n is the refractive, η is the real part of n, S is the transverse area of the waveguide mode, and $(\omega+\omega_0)$ is the photon annihilation operator. For a pulse with a slowly varying envelope compared with the optical carrier frequency, a temporal envelope annihilation operator $\hat{A}(t)$ can be defined as [94]

$$\hat{A}(t) = \frac{1}{\sqrt{2\pi}}\int \mathrm{d}\omega\hat{a}(\omega)e^{-i\omega t}, \tag{27}$$

where

$$\hat{a}(\omega) = \hat{c}(\omega+\omega_0) \tag{28}$$

and $\hat{A}(t)$, $\hat{a}(\omega)$ satisfy the following commutation relations with their corresponding creation operators:

$$[\hat{A}(t), \hat{A}^\dagger(t')] = \delta(t-t'), \tag{29}$$

$$[\hat{a}(\omega), \hat{a}^\dagger(\omega')] = \delta(\omega-\omega'). \tag{30}$$

The evolution of $\hat{A}(t)$ in the fiber can be phenomenologically described by [94–96]

$$\hat{A}_z = -\frac{\alpha}{2}\hat{A} - \frac{i\beta_2}{2}\hat{A}_{tt} + \frac{\beta_3}{6}\hat{A}_{ttt} + \hat{s}, \tag{31}$$

where the subscripts t and z indicate partial derivatives, α is the fiber loss, β_2 is the SOD coefficient, β_3 is the TOD coefficient, and $\hat{s}$ is the Langevin noise operator. In order to maintain the commutation relation Eq. (29), $\hat{s}$ should satisfy

$$[\hat{s}(z,t), \hat{s}^\dagger(z',t')] = \alpha\delta(z-z')\delta(t-t'). \tag{32}$$

We define the pulse COG operator based on Eq. (1) as

$$\hat{T} \equiv \frac{1}{N}\int \mathrm{d}t t\hat{A}^\dagger(t)\hat{A}(t), \tag{33}$$

where

$$N = \left\langle \int \mathrm{d}t\hat{A}^\dagger(t)\hat{A}(t)\right\rangle \tag{34}$$

is the total average photon number. The timing jitter $\mathrm{TJ}(z)$ at position z can then be described by

$$\mathrm{TJ}^2(z) = \langle\hat{T}^2(z)\rangle - \langle\hat{T}(z)\rangle^2. \tag{35}$$

Suppose the optical mode is in a coherent state and the noise reservoir is in the vacuum state; based on Eqs. (29)–(35), we can eventually obtain

$$\begin{aligned}
&\mathrm{TJ}^2(z)\\
&= \langle\hat{T}^2(0)\rangle + \langle\hat{\Omega}^2(0)\rangle\left[\int_0^z \beta_2(z_1)\mathrm{d}z_1\right]^2\\
&+ \frac{1}{4}\langle\hat{\Gamma}^2(0)\rangle\left[\int_0^z \beta_3(z_1)\mathrm{d}z_1\right]^2\\
&+ \langle\hat{T}(0)\hat{\Omega}(0) + \hat{\Omega}(0)\hat{T}(0)\rangle\int_0^z \beta_2(z_1)\mathrm{d}z_1\\
&+ \frac{1}{2}\langle\hat{T}(0)\hat{\Gamma}(0) + \hat{\Gamma}(0)\hat{T}(0)\rangle\int_0^z \beta_3(z_1)\mathrm{d}z_1\\
&+ \frac{1}{2}\langle\hat{\Omega}(0)\hat{\Gamma}(0) + \hat{\Gamma}(0)\hat{\Omega}(0)\rangle\int_0^z \beta_2(z_1)\mathrm{d}z_1\int_0^z \beta_3(z_1)\mathrm{d}z_1\\
&+ 2\int_0^z \mathrm{d}z_1\beta_2(z_1)\int_0^{z_1}\beta_2(z_2)\mathrm{d}z_2\int_0^{z_2}\frac{\alpha(z_3)\Delta\omega^2(z_3)}{N(z_3)})\mathrm{d}z_3\\
&+ \int_0^z \frac{\alpha(z_1)\Delta t^2(z_1)}{N(z_1)}\mathrm{d}z_1\\
&+ \frac{1}{2}\int_0^z \mathrm{d}z_1\beta_3(z_1)\int_0^{z_1}\beta_3(z_2)\mathrm{d}z_2\int_0^{z_2}\frac{\alpha(z_3)D(z_3)}{N(z_3)})\mathrm{d}z_3\\
&+ \int_0^z \mathrm{d}z_1\beta_2(z_1)\int_0^{z_1}\mathrm{d}z_2\frac{\alpha(z_2)C(z_2)}{N(z_2)}\\
&+ \frac{1}{2}\int_0^z \mathrm{d}z_1\beta_3(z_1)\int_0^{z_1}\mathrm{d}z_2\frac{\alpha(z_2)G(z_2)}{N(z_2)}\\
&+ \int_0^z \mathrm{d}z_1\beta_2(z_1)\int_0^{z_1}\beta_3(z_2)\mathrm{d}z_2\int_0^{z_2}\frac{\alpha(z_3)K(z_3)}{N(z_3)})\mathrm{d}z_3,
\end{aligned} \tag{36}$$

where

$$\hat{\Omega}(z) \equiv \frac{1}{N(z)}\int \mathrm{d}t i\hat{A}^\dagger\hat{A}_t, \tag{37}$$

$$\hat{\Gamma}(z) \equiv \frac{1}{N(z)}\int \mathrm{d}t\hat{A}_t^\dagger\hat{A}_t - \left\langle\frac{1}{N(z)}\int \mathrm{d}t\hat{A}_t^\dagger\hat{A}_t\right\rangle, \tag{38}$$

$$\Delta t^2(z) = \left\langle\frac{1}{N(z)}\int \mathrm{d}t t^2\hat{A}^\dagger\hat{A}\right\rangle, \tag{39}$$

$$\begin{aligned}
\Delta\omega^2(z) &= \left\langle\frac{1}{N(z)}\int \mathrm{d}\omega\omega^2\hat{a}^\dagger(\omega)\hat{a}(\omega)\right\rangle\\
&= \left\langle\frac{1}{N(z)}\int \mathrm{d}t\hat{A}_t^\dagger\hat{A}_t\right\rangle,
\end{aligned} \tag{40}$$

$$C(z) = \left\langle\frac{1}{N(z)}\int \mathrm{d}t t i(\hat{A}^\dagger\hat{A}_t - \hat{A}_t^\dagger\hat{A})\right\rangle, \tag{41}$$

$$D(z) = \left\langle\frac{1}{N(z)}\int \mathrm{d}t\hat{A}_{tt}^\dagger\hat{A}_{tt}\right\rangle, \tag{42}$$

$$G(z) = \left\langle-\frac{1}{N(z)}\int \mathrm{d}t t(\hat{A}^\dagger\hat{A}_{tt} + \hat{A}_{tt}^\dagger\hat{A})\right\rangle, \tag{43}$$

$$K(z) = \left\langle\frac{1}{N(z)}\int \mathrm{d}t i(\hat{A}_t^\dagger\hat{A}_{tt} - \hat{A}_{tt}^\dagger\hat{A}_t)\right\rangle. \tag{44}$$

In Eq. (36), the first term is the pulse original jitter limit before fiber transmission, which satisfies the standard quantum limit condition [40]:

$$\langle \hat{T}^2(0)\rangle \geq \frac{\Delta t(0)^2}{N(0)}, \tag{45}$$

where $\Delta t(0)$ is the initial pulse width. The second to sixth terms in Eq. (36) are the "amplified" pulse original jitter through SOD and TOD. The seventh to twelfth terms are the new generated quantum jitter through the coupling between the quantum loss and dispersion effects.

We perform a simulation to investigate how the terms in Eq. (36) affect the timing jitter of optical pulses traveling in fiber links comprised of two sections: PM-1550 and PM-DCF. Starting with a Gaussian pulse of 200-fs FWHM pulse duration, we calculate the timing jitter generated by the quantum noise sources for different pulse energies, fiber link lengths, and residual dispersion values. The calculations shown in Fig. 16(a) are performed for the 3.5-km fiber link in Fig. 14(a) for varying pulse energies. Based on our experimental values, we assume that the link has about 0.1-m worth of residual SOD and 26-m worth of residual TOD in comparison to the dispersion of a 1-m-long PM-1550. As can be seen from the black curve in Fig. 16(a), the total timing jitter generated by the quantum noise sources varies between 180 as RMS and 6 as RMS for pulse energies from 0.1 pJ up to 100 pJ. Due to the large residual TOD, the third term in Eq. (36) generates the largest contribution; [green curve in Fig. 16(a)]. The new generated quantum jitter [red curve in Fig. 16(a)] is also comparable with the pulse initial jitter [blue curve in Fig. 16(a)]. With 4 pJ energy, the total jitter after 3.5-km link transmission is about 26 as.

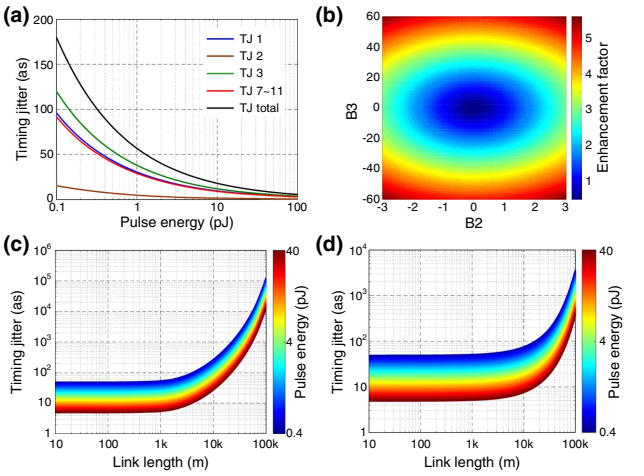

Fig. 16. Analysis of quantum jitter of fiber timing link. The initial pulse has a Gaussian shape with 200-fs FWHM pulse width. The timing link consists of two fiber sections: standard PM fiber PM 1550, and PM DCF. The quantum timing jitter after link transmission is calculated based on Eq. (36). (a) Comparison of jitter contributions with varied input pulse energies. The link is 3.5 km with experimental β_2 and β_3 values. TJ1, 2, 3: the first (pulse original jitter), second ("amplified" jitter through SOD), third term ("amplified" jitter through TOD) in Eq. (36), TJ7 ~ 12: the overall jitter of the seventh to twelfth terms in Eq. (36), TJ total: the overall jitter in Eq. (36). The fourth–sixth and twelfth terms are zero due to the initially unchirped pulse shape. (b) Quantum jitter enhancement through fiber dispersion effects. B2, the link's residual SOD normalized by the SOD of 1-m standard PM 1550; B3, the link's residual TOD normalized by the TOD of 1-m PM 1550. (c) Overall quantum jitter with different link lengths and initial pulse energies; the experimental β_2 and β_3 values are used. (d) Overall quantum jitter with different link lengths and initial pulse energies, B2=0, B3=0.

By varying the β_2 and β_3 of PM-DCF, we also calculate the dispersion-related quantum jitter TJ_D [sum of second to twelfth terms in Eq. (36)] for different residual TOD and SOD values of the fiber link. Furthermore, we determine total jitter from Eq. (36) only under the influence of fiber loss by setting the β_2 and β_3 to zero for both PMF and PM-DCF. Then we can calculate an enhancement factor TJ_D/TJ_L through dispersion, where TJ_L is the overall jitter of Eq. (36). As can be seen in Fig. 16(b), even if the total residual TOD and SOD are zero, an enhanced factor of about 0.51 can be obtained. This suggests that the quantum loss and dispersion are correlated with each other and cannot be treated independently. With 3-m worth of uncompensated SOD and 60-m worth of uncompensated TOD from PM 1550, the quantum jitter can be enhanced by larger than 5 times compared with the no-dispersion case.

The dispersion-induced quantum jitter becomes more serious for longer fiber links. For example, in Fig. 16(c), we use the experimental β_2 and β_3 values, and assume the total link has only 0.1-m worth of uncompensated SOD of PM 1550. As the link length increases, more and more TOD would be uncompensated. When the link length is 100 km, the total quantum jitter is 12.74 fs with 40-pJ pulse energy. If we let both the link residual SOD and TOD to be zero, the total quantum jitter can be reduced to 363 as [Fig. 16(d)]. In Fig. 13(b), we have found that if the pulse energy is below 18 pJ, the timing jitter contributed by fiber nonlinearity is negligible. With this energy level, the total quantum jitter is still below 100 as after 60-km link transmission, if both SOD and TOD are perfectly compensated [Fig. 16(d)].

5. FUTURE DIRECTIONS

There are two possible directions to upgrade large-scale timing synchronization systems: increasing the timing resolution or increasing the timing link length. The timing resolution of a timing synchronization system will eventually be limited by the quantum noise floor of the reference source, timing detector, or link. The timing instability of the timing reference, especially on mode-locked lasers, is limited, as the measured timing jitter nowadays is already close to the predicted quantum limit [33,97]. However, there is still a lot of work that can be done to approach the quantum noise floor of timing detectors. Today, the highest resolution provided by any x-ray timing detector is at a few femtosecond level, which is about 3 orders of magnitude higher than optical timing detectors (e.g., BOC). To resolve the details of a single-shot x-ray pulse, new cross-correlation techniques may be required to implement a more efficient instantaneous pump-probe process between the x-ray pulses and other sources. Two-step cross-correlation may be another solution, e.g., an x-ray pulse first induces a change on an optical probe pulse, which can be further accurately characterized by an optical timing detector, so as to resolve the details of the x-ray pulse. The main noise contribution of optical-microwave phase detectors (such as BOMPD or FLOMPD) is the thermal drift from fibers and RF cables. This noise may be significantly decreased by integrating the phase detector on a single chip. Based on Fig. 3, the BOC noise floor is already very close to the standard quantum limit of the input pulses with an acceptable input power level. The next step may be to directly investigate this quantum limit or even to verify lower limits using squeezed light [95].

The ultimate way to reduce the noise floor of free-space timing links is to put them into vacuum or outer space, which actually

has already been done for gravitational wave detection [98,99]. As indicated by Figs. 13 and 16, to approach the quantum limit of fiber-based timing links, the operating link power needs to be sufficiently low (to remove nonlinear effects), which in turn requires developing higher timing sensitivity optical timing detectors for link stabilization. When the entire timing synchronization system is quantum-noise limited, a large number of similar setups can be operated to perform parallel measurements with the same signal (e.g., gravitational wave) simultaneously, to give another several orders of improvement on the precision after averaging. Finally, the timing link length will be limited by the link loss. Concerning timing links in outer space, gigameter distances may still be possible [99], while for fiber links, larger than hundreds of kilometers can increase the quantum noise floor to above 100 as, if an almost-zero-additive-jitter relay amplifier cannot be provided.

Funding. H2020 European Research Council (ERC); Seventh Framework Programme (FP7) (609920, FP/2007-2013); U.S. Department of Energy (DOE) (DE-SC0011377); Hamburg Centre for Ultrafast Imaging-Structure, Dynamics and Control of Matter at the Atomic Scale of the Deutsche Forschungsgemeinschaft (DFG).

REFERENCES

1. H. A. Haus, "Mode-locking of lasers," IEEE J. Sel. Top. Quantum Electron. **6**, 1173–1185 (2000).
2. D. J. Jones, S. A. Diddams, J. K. Ranka, A. Stentz, R. S. Windeler, J. L. Hall, and S. T. Cundiff, "Carrier-envelope phase control of femtosecond mode-locked lasers and direct optical frequency synthesis," Science **288**, 635–639 (2000).
3. R. Holzwarth, T. Udem, and T. W. Hänsch, "Optical frequency synthesizer for precision spectroscopy," Phys. Rev. Lett. **85**, 2264–2267 (2000).
4. M. Altarelli, R. Brinkmann, M. Chergui, W. Decking, B. Dobson, S. Düsterer, G. Grübel, W. Graeff, H. Graafsma, J. Hajdu, O. Marangos, J. Pflüger, H. Redlin, D. Riley, I. Robinson, J. Rossbach, A. Schwarz, K. Tiedtke, T. Tschentscher, I. Vartaniants, H. Wabnitz, H. Weise, R. Wichmann, K. Witte, A. Wolf, M. Wulff, and M. Yurkov, "XFEL: the European X-ray free-electron laser," Technical Design Report DESY-06-097 2006.
5. E. Allaria, R. Appio, L. Badano, W. A. Barletta, S. Bassanese, S. G. Biedron, A. Borga, E. Busetto, D. Castronovo, P. Cinquegrana, S. Cleva, D. Cocco, M. Cornacchia, P. Craievich, I. Cudin, G. D'Auria, M. Dal Forno, M. B. Danailov, R. De Monte, G. De Ninno, P. Delgiusto, A. Demidovich, S. Di Mitri, B. Diviacco, A. Fabris, R. Fabris, W. Fawley, M. Ferianis, E. Ferrari, S. Ferry, L. Froehlich, P. Furlan, G. Gaio, F. Gelmetti, L. Giannessi, M. Giannini, R. Gobessi, R. Ivanov, E. Karantzoulis, M. Lonza, A. Lutman, B. Mahieu, M. Milloch, S. V. Milton, M. Musardo, I. Nikolov, S. Noe, F. Parmigiani, G. Penco, M. Petronio, L. Pivetta, M. Predonzani, F. Rossi, L. Rumiz, A. Salom, C. Scafuri, C. Serpico, P. Sigalotti, S. Spampinati, C. Spezzani, M. Svandrlik, C. Svetina, S. Tazzari, M. Trovo, R. Umer, A. Vascotto, M. Veronese, R. Visintini, M. Zaccaria, D. Zangrando, and M. Zangrando, "Highly coherent and stable pulses from the FERMI seeded free-electron laser in the extreme ultraviolet," Nat. Photonics **6**, 699–704 (2012).
6. P. Emma, R. Akre, J. Arthur, R. Bionta, C. Bostedt, J. Bozek, A. Brachmann, P. Bucksbaum, R. Coffee, F.-J. Decker, Y. Ding, D. Dowell, S. Edstrom, A. Fisher, J. Frisch, S. Gilevich, J. Hastings, G. Hays, Ph. Hering, Z. Huang, R. Iverson, H. Loos, M. Messerschmidt, A. Miahnahri, S. Moeller, H.-D. Nuhn, G. Pile, D. Ratner, J. Rzepiela, D. Schultz, T. Smith, P. Stefan, H. Tompkins, J. Turner, J. Welch, W. White, J. Wu, G. Yocky, and J. Galayda, "First lasing and operation of an Ångstrom-wavelength free-electron laser," Nat. Photonics **4**, 641–647 (2010).
7. J. Stohr, "Linac coherent light source II (LCLS-II) conceptual design report," Design Report SLAC-R-978(SLAC, 2011).
8. E. Prat and S. Reiche, "Simple method to generate terawatt-attosecond X-ray free-electron-laser pulses," Phys. Rev. Lett. **114**, 244801 (2015).
9. C. Kupitz, S. Basu, I. Grotjohann, R. Fromme, N. A. Zatsepin, K. N. Rendek, M. S. Hunter, R. L. Shoeman, T. A. White, D. Wang, D. James, J. Yang, D. E. Cobb, B. Reeder, R. G. Sierra, H. Liu, A. Barty, A. L. Aquila, D. Deponte, R. A. Kirian, S. Bari, J. J. Bergkamp, K. R. Beyerlein, M. J. Bogan, C. Caleman, T. Chao, C. E. Conrad, K. M. Davis, H. Fleckenstein, L. Galli, S. P. Hau-Riege, S. Kassemeyer, H. Laksmono, M. Liang, L. Lomb, S. Marchesini, A. V. Martin, M. Messerschmidt, D. Milathianaki, K. Nass, A. Ros, S. Roy-Chowdhury, K. Schmidt, M. Seibert, J. Steinbrener, F. Stellato, L. Yan, C. Yoon, T. A. Moore, A. L. Moore, Y. Pushkar, G. J. Williams, S. Boutet, R. B. Doak, U. Weierstall, M. Frank, H. N. Chapman, J. C. H. Spence, and P. Fromme, "Serial time-resolved crystallography of photosystem II using a femtosecond X-ray laser," Nature **513**, 261–265 (2014).
10. H. Öström, H. Öberg, H. Xin, J. LaRue, M. Beye, M. Dell'Angela, J. Gladh, M. L. Ng, J. A. Sellberg, S. Kaya, G. Mercurio, D. Nordlund, M. Hantschmann, F. Hieke, D. Kühn, W. F. Schlotter, G. L. Dakovski, J. J. Turner, M. P. Minitti, A. Mitra, S. P. Moeller, A. Föhlisch, M. Wolf, W. Wurth, M. Persson, J. K. Nørskov, F. Abild-Pedersen, H. Ogasawara, L. G. M. Pettersson, and A. Nilsson, "Probing the transition state region in catalytic CO oxidation on Ru," Science **347**, 978–982 (2015).
11. F. Calegari, D. Ayuso, A. Trabattoni, L. Belshaw, S. De Camillis, S. Anumula, F. Frassetto, L. Poletto, A. Palacios, P. Decleva, J. B. Greenwood, F. Martín, and M. Nisoli, "Ultrafast electron dynamics in phenylalanine initiated by attosecond pulses," Science **346**, 336–339 (2014).
12. S. K. Son, L. Young, and R. Santra, "Impact of hollow-atom formation on coherent x-ray scattering at high intensity," Phys. Rev. A **83**, 033402 (2011).
13. S. P. Hau-Riege, "Photoelectron dynamics in X-ray free-electron-laser diffractive imaging of biological samples," Phys. Rev. Lett. **108**, 238101 (2012).
14. G. Mourou and T. Tajima, "More intense, shorter pulses," Science **331**, 41–42 (2011).
15. R. Betti and O. A. Hurricane, "Inertial-confinement fusion with lasers," Nat. Phys. **12**, 435–448 (2016).
16. G. Mourou, B. Brocklesby, T. Tajima, and J. Limpert, "The future is fibre accelerators," Nat. Photonics **7**, 258–261 (2013).
17. E. Middelberg and U. Bach, "High resolution radio astronomy using very long baseline interferometry," Rep. Prog. Phys. **71**, 066901 (2008).
18. P. E. Dewdney, P. J. Hall, R. T. Schilizzi, and T. J. L. Lazio, "The square kilometre array," Proc. IEEE **97**, 1482–1496 (2009).
19. D. Dravins, T. Lagadec, and P. D. Nuñez, "Optical aperture synthesis with electronically connected telescopes," Nat. Commun. **6**, 6852 (2015).
20. Y. He, K. G. H. Baldwin, B. J. Orr, R. B. Warrington, M. J. Wouters, A. N. Luiten, P. Mirtschin, T. Tzioumis, C. Phillips, J. Stevens, B. Lennon, S. Munting, G. Aben, T. Newlands, and T. Rayner, "Long-distance telecom-fiber transfer of a radio-frequency reference for radio astronomy," Optica **5**, 138–146 (2018).
21. H. A. Haus and A. Mecozzi, "Noise of mode-locked lasers," IEEE J. Quantum Electron. **29**, 983–996 (1993).
22. R. P. Scott, C. Langrock, and B. H. Kolner, "High-dynamic-range laser amplitude and phase noise measurement techniques," IEEE J. Sel. Top. Quantum Electron. **7**, 641–655 (2001).
23. F. Quinlan, T. M. Fortier, H. Jiang, A. Hati, C. Nelson, Y. Fu, J. C. Campbell, and S. A. Diddams, "Exploiting shot noise correlations in the photodetection of ultrashort optical pulse trains," Nat. Photonics **7**, 290–293 (2013).
24. W. Sun, F. Quinlan, T. M. Fortier, J.-D. Deschenes, Y. Fu, S. A. Diddams, and J. C. Campbell, "Broadband noise limit in the photodetection of ultralow jitter optical pulses," Phys. Rev. Lett. **113**, 203901 (2014).
25. L. A. Jiang, S. T. Wong, M. E. Grein, E. P. Ippen, and H. A. Haus, "Measuring timing jitter with optical cross correlations," IEEE J. Quantum Electron. **38**, 1047–1052 (2002).
26. T. R. Schibli, J. Kim, O. Kuzucu, J. T. Gopinath, S. N. Tandon, G. S. Petrich, L. A. Kolodziejski, J. G. Fujimoto, E. P. Ippen, and F. X. Kärtner, "Attosecond active synchronization of passively mode-locked lasers by balanced cross correlation," Opt. Lett. **28**, 947–949 (2003).
27. J. Kim, J. Chen, J. Cox, and F. X. Kärtner, "Attosecond-resolution timing jitter characterization of free-running mode-locked lasers," Opt. Lett. **32**, 3519–3521 (2007).

28. F. X. Kärtner, F. Wong, and J. Kim, "Compact background-free balanced cross-correlators," U.S. patent 7,940,390 B2 (10 May 2011).
29. J. C. Diels and W. Rudolph, *Ultrashort Laser Pulse Phenomena*, 2nd ed. (Academic, 2006).
30. J. A. Cox, A. H. Nejadmalayeri, J. Kim, and F. X. Kärtner, "Complete characterization of quantum-limited timing jitter in passively mode-locked fiber lasers," Opt. Lett. **35**, 3522–3524 (2010).
31. T. K. Kim, Y. Song, K. Jung, C. Kim, H. Kim, C. H. Nam, and J. Kim, "Sub-100-as timing jitter optical pulse trains from mode-locked Er-fiber lasers," Opt. Lett. **36**, 4443–4445 (2011).
32. Y. Song, C. Kim, K. Jung, H. Kim, and J. Kim, "Timing jitter optimization of mode-locked Yb-fiber lasers toward the attosecond regime," Opt. Express **19**, 14518–14525 (2011).
33. A. J. Benedick, J. G. Fujimoto, and F. X. Kärtner, "Optical flywheels with attosecond jitter," Nat. Photonics **6**, 97–100 (2012).
34. K. Şafak, M. Xin, Q. Zhang, S. Chia, O. D. Mücke, and F. X. Kärtner, "Jitter analysis of timing-distribution and remote-laser synchronization systems," Opt. Express **24**, 21752–21766 (2016).
35. H. Li, L.-J. Chen, H. P. H. Cheng, J. E. May, S. Smith, K. Muehlig, A. Uttamadoss, J. C. Frisch, A. R. Fry, F. X. Kärtner, and P. H. Bucksbaum, "Remote two-color optical-to-optical synchronization between two passively mode-locked lasers," Opt. Lett. **39**, 5325–5328 (2014).
36. G. Zhou, M. Xin, F. X. Kärtner, and G. Chang, "Timing jitter of Raman soliton," Opt. Lett. **40**, 5105–5108 (2015).
37. A. H. Nejadmalayeri, F. N. C. Wong, T. D. Roberts, P. Battle, and F. X. Kärtner, "Guided wave optics in periodically poled KTP: quadratic nonlinearity and prospects for attosecond jitter characterization," Opt. Lett. **34**, 2522–2524 (2009).
38. P. T. Callahan, K. Şafak, P. Battle, T. D. Roberts, and F. X. Kärtner, "Fiber-coupled balanced optical cross-correlator using PPKTP waveguides," Opt. Express **22**, 9749–9758 (2014).
39. B. Jones, T. Hawthorne, P. Battle, K. Shtyrkova, M. Xin, P. T. Callahan, F. X. Kärtner, and T. Roberts, "Development of a waveguide-based optical cross-correlator for attosecond timing synchronization," in *Ultrafast Optics (UFO) XI* (2017).
40. V. Giovannetti, S. Lloyd, and L. Maccone, "Quantum enhanced positioning and clock synchronization," Nature **412**, 417–419 (2001).
41. Y. Chen, J. Jiang, and D. J. Jones, "Remote distribution of a mode-locked pulse train with sub 40-as jitter," Opt. Express **14**, 12134–12144 (2006).
42. D. Hou, C.-C. Lee, Z. Yang, and T. R. Schibli, "Timing jitter characterization of mode-locked lasers with <1 zs/$\sqrt{\text{Hz}}$ resolution using a simple optical heterodyne technique," Opt. Lett. **40**, 2985–2988 (2015).
43. D. Kwon, C. Jeon, J. Shin, M. Heo, S. E. Park, Y. Song, and J. Kim, "Reference-free, high-resolution measurement method of timing jitter spectra of optical frequency combs," Sci. Rep. **7**, 40917 (2017).
44. J. Kim, F. X. Kärtner, and F. Ludwig, "Balanced optical-microwave phase detectors for optoelectronic phase-locked loops," Opt. Lett. **31**, 3659–3661 (2006).
45. J. Kim, J. A. Cox, J. Chen, and F. X. Kärtner, "Drift-free femtosecond timing synchronization of remote optical and microwave sources," Nat. Photonics **2**, 733–736 (2008).
46. M. Y. Peng, A. Kalaydzhyan, and F. X. Kärtner, "Balanced optical-microwave phase detector for sub-femtosecond optical-RF synchronization," Opt. Express **22**, 27102–27111 (2014).
47. M. Xin, K. Şafak, M. Y. Peng, A. Kalaydzhyan, W. Wang, O. D. Mücke, and F. X. Kärtner, "Attosecond precision multi-kilometer laser-microwave network," Light Sci. Appl. **6**, e16187 (2017).
48. K. Jung and J. Kim, "Sub-femtosecond synchronization of microwave oscillators with mode-locked Er-fiber lasers," Opt. Lett. **37**, 2958–2960 (2012).
49. H. Yang, B. Han, J. Shin, D. Hou, H. Chung, I. H. Baek, Y. U. Jeong, and J. Kim, "10-fs-level synchronization of photocathode laser with RF-oscillator for ultrafast electron and X-ray sources," Sci. Rep. **7**, 39966 (2017).
50. M. Endo, T. D. Shoji, and T. R. Schibli, "High-sensitivity optical to microwave comparison with dual-output Mach-Zehnder modulators," Sci. Rep. **8**, 4388 (2018).
51. C. Jeon, Y. Na, B. Lee, and J. Kim, "Simple-structured, subfemtosecond-resolution optical-microwave phase detector," Opt. Lett. **43**, 3997–4000 (2018).
52. M. Lessing, H. S. Margolis, C. T. A. Brown, P. Gill, and G. Marra, "Suppression of amplitude-to-phase noise conversion in balanced optical-microwave phase detectors," Opt. Express **21**, 27057–27062 (2013).
53. F. N. Baynes, F. Quinlan, T. M. Fortier, Q. Zhou, A. Beling, J. C. Campbell, and S. A. Diddams, "Attosecond timing in optical-to-electrical conversion," Optica **2**, 141–146 (2015).
54. R. Bouchand, D. Nicolodi, X. Xie, C. Alexandre, and Y. L. Coq, "Accurate control of optoelectronic amplitude to phase noise conversion in photodetection of ultra-fast optical pulses," Opt. Express **25**, 12268–12281 (2017).
55. Y. Ding, F.-J. Decker, P. Emma, C. Feng, C. Field, J. Frisch, Z. Huang, J. Krzywinski, H. Loos, J. Welch, J. Wu, and F. Zhou, "Femtosecond x-ray pulse characterization in free-electron lasers using a cross-correlation technique," Phys. Rev. Lett. **109**, 254802 (2012).
56. A. L. Cavalieri, D. M. Fritz, S. H. Lee, P. H. Bucksbaum, D. A. Reis, J. Rudati, D. M. Mills, P. H. Fuoss, G. B. Stephenson, C. C. Kao, D. P. Siddons, D. P. Lowney, A. G. MacPhee, D. Weinstein, R. W. Falcone, R. Pahl, J. Als-Nielsen, C. Blome, S. Düsterer, R. Ischebeck, H. Schlarb, H. Schulte-Schrepping, Th. Tschentscher, J. Schneider, O. Hignette, F. Sette, K. Sokolowski-Tinten, H. N. Chapman, R. W. Lee, T. N. Hansen, O. Synnergren, J. Larsson, S. Techert, J. Sheppard, J. S. Wark, M. Bergh, C. Caleman, G. Huldt, D. van der Spoel, N. Timneanu, J. Hajdu, R. A. Akre, E. Bong, P. Emma, P. Krejcik, J. Arthur, S. Brennan, K. J. Gaffney, A. M. Lindenberg, K. Luening, and J. B. Hastings, "Clocking femtosecond X Rays," Phys. Rev. Lett. **94**, 114801 (2005).
57. F. Tavella, N. Stojanovic, G. Geloni, and M. Gensch, "Few-femtosecond timing at fourth-generation X-ray light sources," Nat. Photonics **5**, 162–165 (2011).
58. C. Gahl, A. Azima, M. Beye, M. Deppe, K. Döbrich, U. Hasslinger, F. Hennies, A. Melnikov, M. Nagasono, A. Pietzsch, M. Wolf, W. Wurth, and A. Föhlisch, "A femtosecond X-ray/optical cross-correlator," Nat. Photonics **2**, 165–169 (2008).
59. M. Harmand, R. Coffee, M. R. Bionta, M. Chollet, D. French, D. Zhu, D. M. Fritz, H. T. Lemke, N. Medvedev, B. Ziaja, S. Toleikis, and M. Cammarata, "Achieving few-femtosecond time-sorting at hard X-ray free-electron lasers," Nat. Photonics **7**, 215–218 (2013).
60. I. Grguraš, A. R. Maier, C. Behrens, T. Mazza, T. J. Kelly, P. Radcliffe, S. Düsterer, A. K. Kazansky, N. M. Kabachnik, Th. Tschentscher, J. T. Costello, M. Meyer, M. C. Hoffmann, H. Schlarb, and A. L. Cavalieri, "Ultrafast X-ray pulse characterization at free-electron lasers," Nat. Photonics **6**, 852–857 (2012).
61. S. Schulz, I. Grguraš, C. Behrens, H. Bromberger, J. T. Costello, M. K. Czwalinna, M. Felber, M. C. Hoffmann, M. Ilchen, H. Y. Liu, T. Mazza, M. Meyer, S. Pfeiffer, P. Prędki, S. Schefer, C. Schmidt, U. Wegner, H. Schlarb, and A. L. Cavalieri, "Femtosecond all-optical synchronization of an X-ray free-electron laser," Nat. Commun. **6**, 5938 (2015).
62. P. Cinquegrana, S. Cleva, A. Demidovich, G. Gaio, R. Ivanov, G. Kurdi, I. Nikolov, P. Sigalotti, and M. B. Danailov, "Optical beam transport to a remote location for low jitter pump-probe experiments with a free electron laser," Phys. Rev. ST Accel. Beams **17**, 040702 (2014).
63. M. C. Divall, P. Mutter, E. J. Divall, and C. P. Hauri, "Femtosecond resolution timing jitter correction on a TW scale Ti:sapphire laser system for FEL pump-probe experiments," Opt. Express **23**, 29929–29939 (2015).
64. A. Casanova, Q. D'Acremont, G. Santarelli, S. Dilhaire, and A. Courjaud, "Ultrafast amplifier additive timing jitter characterization and control," Opt. Lett. **41**, 898–900 (2016).
65. M. Pergament, G. Palmer, M. Kellert, K. Kruse, J. Wang, L. Wissmann, U. Wegner, M. Emons, D. Kane, G. Priebe, S. Venkatesan, T. Jezynski, F. Pallas, and M. J. Lederer, "Versatile optical laser system for experiments at the European X-ray free-electron laser facility," Opt. Express **24**, 29349–29359 (2016).
66. S. Valente, A.-L. Calendron, J. Meier, E. Kueny, H. Cankaya, N. H. Matlis, G. Cirmi, and F. X. Kärtner, "Timing stabilization of solid-state, Yb-based laser system," in *Conference on Lasers & Electro-Optics (CLEO)* (2018), paper JTh2A.140.
67. J. Kang, J. Shin, C. Kim, K. Jung, S. Park, and J. Kim, "Few-femtosecond-resolution characterization and suppression of excess timing jitter and drift in indoor atmospheric frequency comb transfer," Opt. Express **22**, 26023–26031 (2014).

68. F. Sun, D. Hou, D. Zhang, J. Tian, J. Hu, X. Huang, and S. Chen, "Femtosecond-level timing fluctuation suppression in atmospheric frequency transfer with passive phase conjunction correction," Opt. Express **25**, 21312–21320 (2017).
69. F. R. Giorgetta, W. C. Swann, L. C. Sinclair, E. Baumann, I. Coddington, and N. R. Newbury, "Optical two-way time and frequency transfer over free space," Nat. Photonics **7**, 434–438 (2013).
70. J. Lee, Y. Kim, K. Lee, S. Lee, and S. Kim, "Time-of-flight measurement with femtosecond light pulses," Nat. Photonics **4**, 716–720 (2010).
71. J. D. Deschênes, L. C. Sinclair, F. R. Giorgetta, W. C. Swann, E. Baumann, H. Bergeron, M. Cermak, I. Coddington, and N. R. Newbury, "Synchronization of distant optical clocks at the femtosecond level," Phys. Rev. X **6**, 021016 (2016).
72. H. Bergeron, L. C. Sinclair, W. C. Swann, C. W. Nelson, J.-D. Deschênes, E. Baumann, F. R. Giorgetta, I. Coddington, and N. R. Newbury, "Tight real-time synchronization of a microwave clock to an optical clock across a turbulent air path," Optica **3**, 441–447 (2016).
73. L. C. Sinclair, H. Bergeron, W. C. Swann, E. Baumann, J.-D. Deschênes, and N. R. Newbury, "Comparing optical oscillators across the air to milliradians in phase and 10^{-17} in frequency," Phys. Rev. Lett. **120**, 050801 (2018).
74. I. Coddington, W. C. Swann, L. Lorini, J. C. Bergquist, Y. Le Coq, C. W. Oates, Q. Quraishi, K. S. Feder, J. W. Nicholson, P. S. Westbrook, S. A. Diddams, and N. R. Newbury, "Coherent optical link over hundreds of metres and hundreds of terahertz with subfemtosecond timing jitter," Nat. Photonics **1**, 283–287 (2007).
75. S. Foreman, A. Ludlow, M. Miranda, J. Stalnaker, S. Diddams, and J. Ye, "Coherent optical phase transfer over a 32-km fiber with 1 s instability at 10^{-17}," Phys. Rev. Lett. **99**, 153601 (2007).
76. O. Lopez, A. Amy-Klein, M. Lours, C. Chardonnet, and G. Santarelli, "High-resolution microwave frequency dissemination on an 86-km urban optical link," Appl. Phys. B **98**, 723–727 (2010).
77. K. Predehl, G. Grosche, S. M. F. Raupach, S. Droste, O. Terra, J. Alnis, T. Legero, T. W. Hänsch, T. Udem, R. Holzwarth, and H. Schnatz, "A 920-kilometer optical fiber link for frequency metrology at the 19th decimal place," Science **336**, 441–444 (2012).
78. R. Wilcox, J. M. Byrd, L. Doolittle, G. Huang, and J. W. Staples, "Stable transmission of radio frequency signals on fiber links using interferometric delay sensing," Opt. Lett. **34**, 3050–3052 (2009).
79. J. M. Glownia, J. Cryan, J. Andreasson, A. Belkacem, N. Berrah, C. I. Blaga, C. Bostedt, J. Bozek, L. F. DiMauro, L. Fang, J. Frisch, O. Gessner, M. Gühr, J. Hajdu, M. P. Hertlein, M. Hoener, G. Huang, O. Kornilov, J. P. Marangos, A. M. March, B. K. McFarland, H. Merdji, V. S. Petrovic, C. Raman, D. Ray, D. A. Reis, M. Trigo, J. L. White, W. White, R. Wilcox, L. Young, R. N. Coffee, and P. H. Bucksbaum, "Time-resolved pump-probe experiments at the LCLS," Opt. Express **18**, 17620–17630 (2010).
80. J. Kim, J. Chen, Z. Zhang, F. N. C. Wong, F. X. Kärtner, F. Loehl, and H. Schlarb, "Long-term femtosecond timing link stabilization using a single-crystal balanced cross correlator," Opt. Lett. **32**, 1044–1046 (2007).
81. M. Y. Peng, P. T. Callahan, A. H. Nejadmalayeri, S. Valente, M. Xin, L. Grüner-Nielsen, E. M. Monberg, M. Yan, J. M. Fini, and F. X. Kärtner, "Long-term stable, sub-femtosecond timing distribution via a 1.2-km polarization-maintaining fiber link: approaching 10^{-21} link stability," Opt. Express **21**, 19982–19989 (2013).
82. K. Şafak, M. Xin, P. T. Callahan, M. Y. Peng, and F. X. Kärtner, "All fiber-coupled, long-term stable timing distribution for free electron lasers with few-femtosecond jitter," Struct. Dyn. **2**, 041715 (2015).
83. M. Xin, K. Şafak, M. Y. Peng, P. T. Callahan, A. Kalaydzhyan, W. Wang, K. Shtyrkova, Q. Zhang, S.-H. Chia, B. Jones, T. Hawthorne, P. Battle, O. D. Mücke, T. Roberts, and F. X. Kärtner, "Sub-fs precision timing synchronization systems," Nucl. Instrum. Methods Phys. Res. Sect. A **907**, 169–181 (2018).
84. G. P. Agrawal, *Nonlinear Fiber Optics*, 4th ed. (Academic, 2013).
85. J. Hult, "A fourth-order Runge–Kutta in the interaction picture method for simulating supercontinuum generation in optical fibers," J. Lightwave Technol. **25**, 3770–3775 (2007).
86. J. P. Gordon and H. A. Haus, "Random walk of coherently amplified solitons in optical fiber transmission," Opt. Lett. **11**, 665–667 (1986).
87. M. Xin, K. Şafak, M. Y. Peng, P. T. Callahan, and F. X. Kärtner, "One-femtosecond, long-term stable remote laser synchronization over a 3.5-km fiber link," Opt. Express **22**, 14904–14912 (2014).
88. K. Jung, J. Shin, J. Kang, S. Hunziker, C. Min, and J. Kim, "Frequency comb-based microwave transfer over fiber with 7×10^{-19} instability using fiber-loop optical-microwave phase detectors," Opt. Lett. **39**, 1577–1580 (2014).
89. M. Xin, K. Şafak, M. Y. Peng, A. Kalaydzhyan, P. T. Callahan, W. Wang, O. D. Mücke, and F. X. Kärtner, "Breaking the femtosecond barrier in multi-km timing synchronization system," IEEE J. Sel. Top. Quantum Electron. **23**, 8800212 (2017).
90. K. Şafak, M. Xin, M. Y. Peng, and F. X. Kärtner, "Synchronous multi-color laser network with daily sub-femtosecond timing drift," Sci. Rep. **8**, 11948 (2018).
91. W. Wang, A. Kalaydzhyan, K. Şafak, M. Xin, M. Y. Peng, K. Jung, J. Kim, and F. X. Kärtner, "High precision synchronization of a large-scale microwave network over stabilized fiber links," in *Conference on Lasers and Electro-Optics (CLEO)* (2016), paper SM4H.5.
92. A. Kalaydzhyan, M. Y. Peng, M. Xin, K. Şafak, W. Wang, and F. X. Kärtner, "Optical-to-microwave synchronization with sub-femtosecond daily drift," in *30th European Frequency and Time Forum (EFTF)* (2016).
93. B. Huttner and S. M. Barnett, "Quantization of the electromagnetic field in dielectrics," Phys. Rev. A **46**, 4306–4322 (1992).
94. M. Tsang, "Decoherence of quantum-enhanced timing accuracy," Phys. Rev. A **75**, 063809 (2007).
95. S. J. Carter, P. D. Drummond, M. D. Reid, and R. M. Shelby, "Squeezing of quantum solitons," Phys. Rev. Lett. **58**, 1841–1844 (1987).
96. M. O. Scully, M. S. Zubairy, and I. A. Walmsley, *Quantum Optics* (Cambridge University, 1997).
97. H. Kim, P. Qin, Y. Song, H. Yang, J. Shin, C. Kim, K. Jung, C. Wang, and J. Kim, "Sub-20-attosecond timing jitter mode-locked fiber lasers," IEEE J. Sel. Top. Quantum Electron. **20**, 0901108 (2014).
98. B. P. Abbott, (LIGO Scientific Collaboration and Virgo Collaboration), "Observation of gravitational waves from a binary black hole merger," Phys. Rev. Lett. **116**, 061102 (2016).
99. P. A. Seoane, S. Aoudia, S. Babak, P. Binétruy, E. Berti, A. Bohé, C. Caprini, M. Colpi, N. J. Cornish, K. Danzmann, J.-F. Dufaux, J. Gair, O. Jennrich, P. Jetzer, A. Klein, R. N. Lang, A. Lobo, T. Littenberg, S. T. McWilliams, G. Nelemans, A. Petiteau, E. K. Porter, B. F. Schutz, A. Sesana, R. Stebbins, T. Sumner, M. Vallisneri, S. Vitale, M. Volonteri, and H. Ward, "Low-frequency gravitational-wave science with eLISA/NGO," Class. Quantum Grav. **29**, 124016 (2012).